

Ultra-fast image sensor using Ge on insulator MIS/Schottky detectors

Chee-Wee Liu

Prof., Department of Electrical Engineering, National Taiwan University,

No.1 Sec.4 Roosevelt Rd. Taipei, Taiwan, R. O. C.

Tel: +886-2-23635251 ext. 515 Fax: +886-2-23640076

<http://nanosioe.ee.ntu.edu.tw> email: chee@cc.ee.ntu.edu.tw

Abstract

The Ge-on-insulator has been fabricated by wafer bonding and smart-cut. The MIS structure leads to simple fabrication process as compared to the conventional PIN structure. Due to the small bandgap of Ge, 1.3 μm and 1.55 μm infrared beside 850 nm can be detected. The low parasitics of GOI structure also increase the detection speed. The large work function metal (Pt) is used for the gate electrode to reduce the dark current of the MIS tunneling diode. Chemical etching is an effective method to remove the implantation damage in order to reduce the dark current and increase the responsivities of visible light. The major achievements are: 1) Thin film Ge on oxide on Si has been demonstrated with smart-cut and wafer bonding at low temperature as low as 150 $^{\circ}\text{C}$, and the detector has been fabricated using simple MIS structure. 2) Responsivity up to 0.2 A/W can be obtained for 850 nm and 1.3 μm infrared. 3) The dark current of the GOI MIS detector at -2 V can be decreased by a factor of 18 as compared to the GOI SB detector. 4) External mechanical strain can further enhance the photo current, while the dark current variation is smaller than 2 %. 5) Higher operational speed can be achieved with a Ge-on-insulator detector as compared to the bulk Ge detector. 6) Thin film Ge can be used for visible light detection. The red- and green- responses have been measured.

Report Documentation Page				Form Approved OMB No. 0704-0188	
Public reporting burden for the collection of information is estimated to average 1 hour per response, including the time for reviewing instructions, searching existing data sources, gathering and maintaining the data needed, and completing and reviewing the collection of information. Send comments regarding this burden estimate or any other aspect of this collection of information, including suggestions for reducing this burden, to Washington Headquarters Services, Directorate for Information Operations and Reports, 1215 Jefferson Davis Highway, Suite 1204, Arlington VA 22202-4302. Respondents should be aware that notwithstanding any other provision of law, no person shall be subject to a penalty for failing to comply with a collection of information if it does not display a currently valid OMB control number.					
1. REPORT DATE 28 MAY 2008		2. REPORT TYPE Final		3. DATES COVERED 01-07-2006 to 30-06-2007	
4. TITLE AND SUBTITLE Ultra-fast image sensor using Ge on insulator Schottky/MIS detectors				5a. CONTRACT NUMBER FA48690610068	
				5b. GRANT NUMBER	
				5c. PROGRAM ELEMENT NUMBER	
6. AUTHOR(S) Cheewee Liu				5d. PROJECT NUMBER	
				5e. TASK NUMBER	
				5f. WORK UNIT NUMBER	
7. PERFORMING ORGANIZATION NAME(S) AND ADDRESS(ES) National Taiwan University, No 1 Sec 4 Roosevelt, Taipei, Taiwan, NA, 106				8. PERFORMING ORGANIZATION REPORT NUMBER N/A	
9. SPONSORING/MONITORING AGENCY NAME(S) AND ADDRESS(ES) AOARD, UNIT 45002, APO, AP, 96337-5002				10. SPONSOR/MONITOR'S ACRONYM(S) AOARD	
				11. SPONSOR/MONITOR'S REPORT NUMBER(S) AOARD-064069	
12. DISTRIBUTION/AVAILABILITY STATEMENT Approved for public release; distribution unlimited					
13. SUPPLEMENTARY NOTES					
14. ABSTRACT The Ge-on-insulator has been fabricated by wafer bonding and smart-cut. The MIS structure leads to simple fabrication process as compared to the conventional PIN structure. Due to the small band gap of Ge, 1.3 &#956;m and 1.55 &#956;m infrared beside 850 nm can be detected. The low parasitics of GOI structure also increase the detection speed. The large work function metal (Pt) is used for the gate electrode to reduce the dark current of the MIS tunneling diode. Chemical etching is an effective method to remove the implantation damage in order to reduce the dark current and increase the responsivities of visible light. The major achievements are: 1) Thin film Ge on oxide on Si has been demonstrated with smart-cut and wafer bonding at low temperature as low as 150 oC, and the detector has been fabricated using simple MIS structure. 2) Responsivity up to 0.2 A/W can be obtained for 850 nm and 1.3 &#956;m infrared. 3) The dark current of the GOI MIS detector at -2 V can be decreased by a factor of 18 as compared to the GOI SB detector. 4) External mechanical strain can further enhance the photo current, while the dark current variation is smaller than 2 %. 5) Higher operational speed can be achieved with a Ge-on-insulator detector as compared to the bulk Ge detector. 6) Thin film Ge can be used for visible light detection. The red- and green- responses have been measured.					
15. SUBJECT TERMS					
16. SECURITY CLASSIFICATION OF:			17. LIMITATION OF ABSTRACT Same as Report (SAR)	18. NUMBER OF PAGES 25	19a. NAME OF RESPONSIBLE PERSON
a. REPORT unclassified	b. ABSTRACT unclassified	c. THIS PAGE unclassified			

Introduction

Ge with bandgap of 0.66 eV and direct bandgap of 0.8 eV is a promising material for visible and infrared ultra-fast detectors since only a thin film Ge is needed. The Ge layer much thicker than absorption length is also not desirable due to costly Ge layers. Photonic devices with Si-on-insulator (SOI) structure are of great interest in recent years [1]. The SOI structure can improve the performance of the CMOS circuits due to the reduction of parasitic capacitance. However, due to Si bandgap, the near infrared at the optical communication wavelength of 1.3 μm and 1.55 μm can not be detected. The Ge-on-insulator (GOI) on Si substrates can potentially lower the cost, and the inherent low parasitics of the GOI structure can increase the speed. Ge p-i-n photodetector have been demonstrated with Ge directly grown on SOI [2] or Si [3] substrates. In this report, we investigate GOI metal-insulator-semiconductor (MIS) photodetectors by wafer bonding and smart-cut [4]. The GOI fabrication was demonstrated at low-temperature as low as 150°C. To the best of our knowledge, this is the lowest GOI process temperature has ever demonstrated. The advantages of hydrogen effects on low-temperature GOI fabrication process such as the smoother cleaved surface and defect passivation were observed. The MIS detector can have a lower dark current density and a simple process without n and p dopant implantation or diffusion. To demonstrate the advantage of GOI MIS detectors, a GOI Schottky barrier (SB) detector is also studied with a structure similar to the GOI MIS detector without LPD oxide. At -2 V bias, the dark current density of the GOI MIS detector is 0.23 A/cm², while the dark current density of the GOI SB detector is 4.2 A/cm². The large work function metal (Pt) is used for the gate electrode to reduce the dark current. The responsivity of 0.23 A/W at the wavelength of 1.3 μm was achieved using n-type Ge with the thickness of 1.3 μm . External mechanical strain can further enhance the photocurrent with only slight degradation of the dark current. The red- and green- responses are also measured. The thin film Ge detectors can be used for the system-on-panel applications.

GOI MIS detectors

The n-type, 1-30 $\Omega\text{-cm}$ (001) Ge substrate was prepared as a “host” wafer. The H⁺ ions with a dose of 1~1.5 $\times 10^{17}$ cm⁻² and the energy of 150~200 keV were implanted into the host wafer to form a deep weakened layer (Step 1 in Fig. 1). On the other wafer, 50~80 nm thermal oxide was grown on the p-Si to form the “handle” wafer. The handle wafer and host wafer were hydrophilically cleaned in the NH₄OH : H₂O₂ : H₂O solution and KOH : H₂O solution, respectively (Step 2 in Fig. 1). After being rinsed in DI water, the wafer pair were initially bonded, and then annealed to strengthen the chemical bonds between the faces of the two

wafers and to induce layer transfer along the weakened hydrogen-implanted regions by H₂ blistering (Step 3 in Fig. 1). Different pairs have been fabricated at annealing temperature from 150 to 300°C for comparison. Al with a ring area was evaporated on Ge. Since the Al ohmic contact has a large area ($>0.1 \text{ cm}^2$) and the barrier height between Al and Ge is small (0.1 eV), the effect of contact resistance is small [5]. The low-temperature (50°C) liquid phase deposited (LPD) oxide [6] and Pt gate were used as the gate stack inside the Al ring (Step 4 in Fig. 1). Fig. 2 shows the cross-sectional transmission electron micrograph (TEM) of the GOI MIS detector.

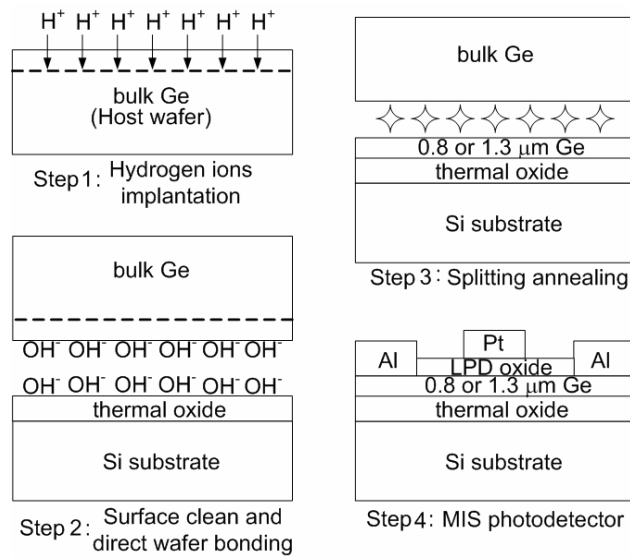


Fig. 1 The process flow of GOI MIS photodetector demonstration.

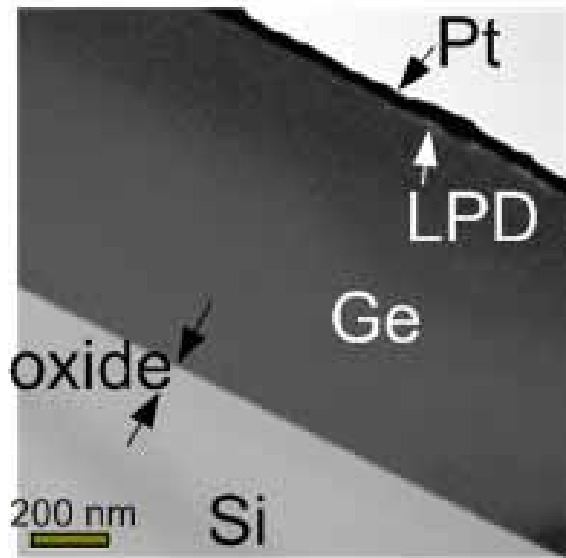


Fig. 2 The cross-sectional transmission electron micrograph (TEM) of the GOI MIS photodetector.

According to experimental results published in the literature [7], hydrogen is the fast diffuser in germanium. The hydrogen can diffuse out of surface during the bonding process, especially at the instant of breakage. The lower process temperature produces more concentrated hydrogen profile because of the low diffusion coefficient of hydrogen at low temperature. The concentrated hydrogen region would lead to a smooth cleaved surface since the separation along the microcavity plane during the smart-cut process is generated by the hydrogen bubbling near the peak implantation region (Fig. 3). The pressure inside the microcavity becomes the driving force for the layer separation. Fig. 4 shows surface roughness of the GOI samples as the function of process temperatures, measured by AFM on $1\mu\text{m} \times 1\mu\text{m}$ area. It shows that surface roughness continues to decrease as process temperature decreases. The separated surfaces exhibit a root-mean-square roughness of $\sim 7 \text{ nm}$ after the H₂ blistering at 150°C for 12 hr, while the roughness is as high as $\sim 27 \text{ nm}$ at the bonding of

300°C for 12 hr.

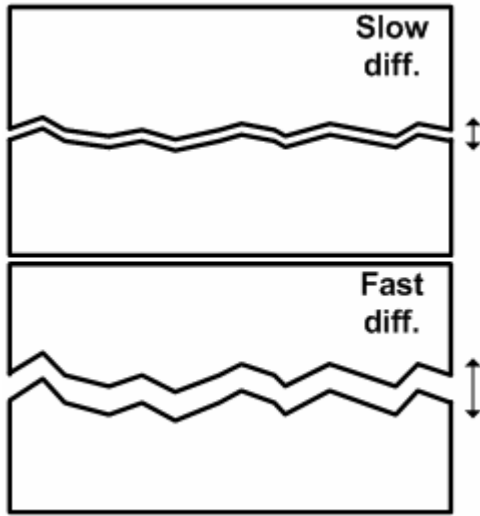


Fig. 3 The lower process temperature produces more concentrated hydrogen profile and a smoother cleaved surface because of the lower diffusion coefficient of hydrogen at lower temperature.

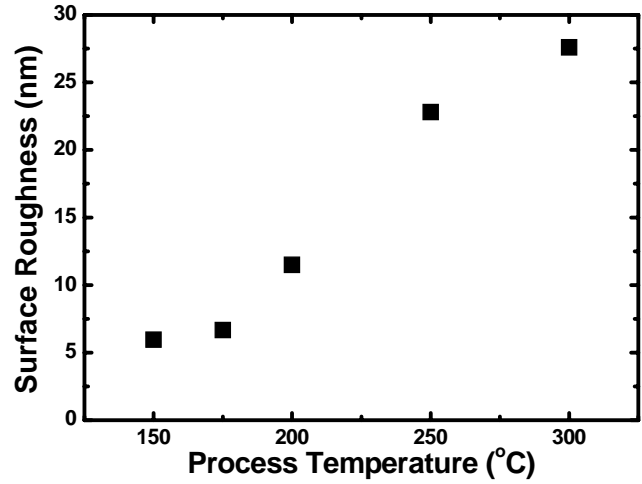


Fig. 4 Surface roughness as a function of process temperature. The separated surfaces surface roughness continues to decrease as process temperature decreases.

At negative bias, the thermal generated electron-hole pairs via defects at the Ge/SiO₂ interface and in the depletion region of Ge are swept separately by the electric field and form the dark current. Under infrared exposure at inversion bias, the excess electron-hole pairs are generated in semiconductor and contribute to the photocurrent. The currents of the 0.8- μ m-thick-Ge GOI MIS detector are shown in Fig. 5. Because the Pt gate electrode would block and reflect the light shined directly on the device, the fiber was pointed to the edge of the gate electrode and the photo-generated carriers can be collected by the electrode due to lateral diffusion and drift of the carriers. At -2 V, the responsivities at 850 nm, 1.3 μ m, and 1.55 μ m are 0.22 A/W, 0.19 A/W, and 0.04 A/W, respectively.

Fig. 6 shows the photoresponses of GOI MIS diodes under light exposure at the wavelength of 850 nm at different bonding temperatures. The photo-generated holes and electrons in the deep depletion region are separately swept toward the Pt and Al electrodes, respectively, to form the photo currents. The photo-generated carriers may be trapped in defects and leads low responsivity. During thermal treatment, the implanted hydrogen ions can passivate the defects created by implantation damages in the Ge. At lower bonding temperature, the diffusion of hydrogen ions out of the wafers can be suppressed and more hydrogen can passivate the damage defects. Fig. 6 shows that the responsivity increase from 0.0036 A/W to 0.22 A/W as the process temperature decreases from 300°C to 150°C. This

indicates that the implantation induced damage defects were effectively passivated by hydrogen ions at low-temperature process. Note that as the process temperature decreases, the gate leakage current decreases. The leakage current of MIS tunneling diode at inversion bias (negative bias for n-type Ge) is dominated by thermal generation of electron-hole pairs through the defects in the depletion region and at the Ge/oxide interface. The lower defect density at lower bonding temperature due to the hydrogen passivation of implantation defects can therefore reduce the leakage current.

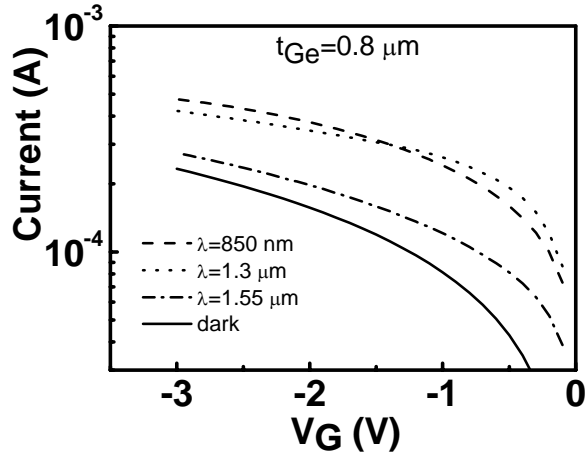


Fig. 5 The dark and 850nm, 1.3 μm , and 1.55 μm infrared photocurrent vs. voltage (I-V) characteristic for the detector with 0.8 μm Ge.

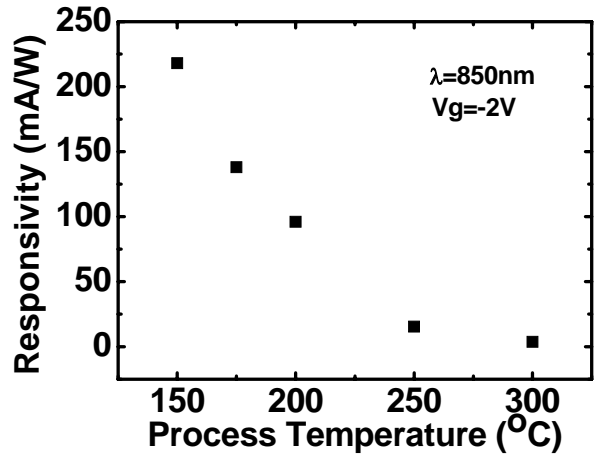


Fig. 6 The 850 nm infrared responsivities of GOI detectors at different process temperatures. The responsivity increases as the process temperature decreases.

To increase the responsivity at 1.3 μm infrared, thicker Ge is fabricated. The currents of the 1.3- μm -thick-Ge GOI MIS detector are shown in Fig. 7. At -2 V, the responsivity of 1.3 μm infrared of the 1.3- μm -thick-Ge GOI MIS detector is 0.23 A/W, which increases 24% as compared to the 0.8- μm -thick-Ge sample.

MIS/Schottky detectors

The MIS detector can have a lower dark current and a simple process without n and p dopant implantation or diffusion. To demonstrate the advantage of GOI MIS detectors, a GOI Schottky barrier (SB) detector is also studied with a structure similar to the GOI MIS detector without LPD oxide. Due to the fast trap-assisted tunneling through the LPD oxide, the dark inversion current of the MIS device is dominated by the thermal generation rate of electron-hole pairs via interface traps and the traps in the deep depletion region of Ge [8], while for the SB diodes, the dark current is dominated by the thermionic emission current from Pt to Ge [9]. At -2 V bias, the dark current density of the GOI MIS detector is 0.23

A/cm², while the dark current density of the GOI SB detector is 4.2 A/cm². Meanwhile, the MIS detector has 1.3 μm wavelength responsivity of 0.23 A/W larger than the SB detector (0.16 A/W). For comparison with the other reports, the dark current of MSM [10] and PIN [2] detectors are 0.3 A/cm² and 0.4 A/cm², respectively, at 2V bias. Due to implantation damage, our SB detector has a large dark current, but MIS structure reduces the dark current. The dark current of our MIS detectors can be further reduced by removing the interface states between insulator and Ge as well as implantation damage.

The barrier height of Pt SB detector on the rough surface of Ge after smart-cut, measured by IV and CV, is about 0.5 eV, corresponding to the effective Pt work function of 4.6 eV, and the low effective Pt work function leads to much higher dark current of the Pt SB device than the Pt MIS device. The defects after the smart-cut may be responsible for the work function reduction due to Fermi level pinning. Therefore, the GOI SB detector has 18 times dark current of the GOI MIS detector at the negative bias of 2 V.

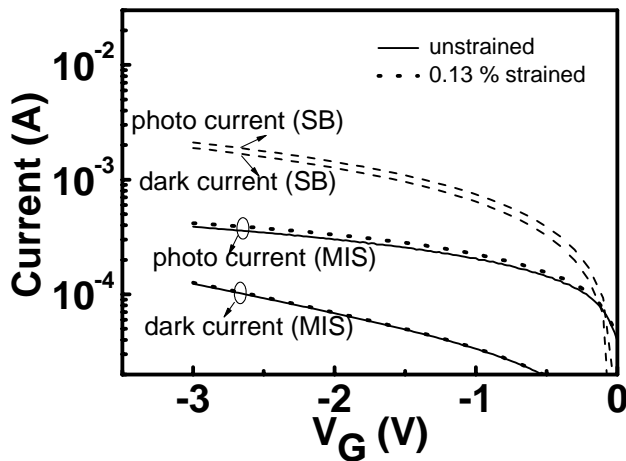


Fig. 7 The photo (1.3 μm infrared) and dark currents of the unstrained or strained GOI MIS detector with a 1.3- μm -thick-Ge layer. The currents of the unstrained SB detector are also shown for comparison.

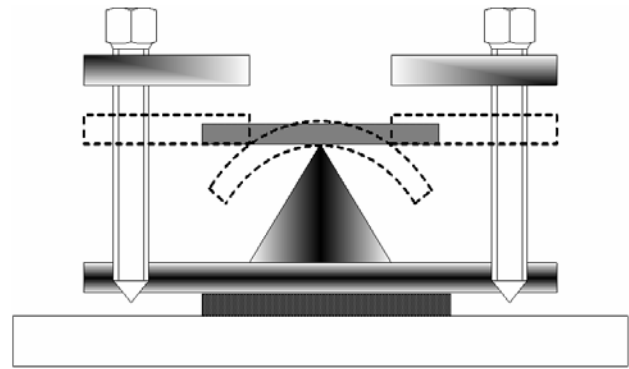


Fig. 8 The mechanism for applying external mechanical strain on the device. The level of strain is determined by the four screws on each corner of the square washer.

Mechanical strain on detectors

The photocurrent of the GOI MIS detector can be enhanced by applying external mechanical strain on the device. The strain mechanism used in this work is shown in Fig. 8. The photocurrent enhancement can reach 11 % at 0.13 % biaxial tensile strain (Fig. 9). The dark current variation is smaller than 2 %, since it is only dominated by defects, which do not change under strain. The increase of photocurrent is mostly due to the strain-induced bandgap narrowing [11] (Fig. 10). The smaller bandgap contributes to shorter absorption depth and

leads to more effective absorption.

Higher operational speed

The 850 nm transient response measurement of the 0.8- μm -thick-Ge GOI detector at -2V shows 60 % enhancement of bandwidth as compared to the bulk Ge detector (Fig. 11). The large area ($3 \times 10^{-4} \text{ cm}^2$) leads to a small bandwidth of 540 MHz of our GOI detector due to RC delay. The capacitance of 1.8 pF and the series resistance of 150Ω can be extracted from the S-parameter, and the RC-limit bandwidth is 590 MHz, close to the measured bandwidth. The MIS structure can form a deep depletion region in the Ge thin film, and the capacitance due to depletion region is in series with gate oxide capacitance to reduce the total capacitance.

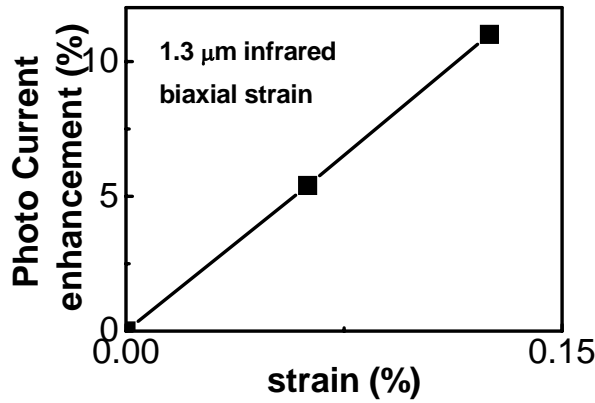


Fig. 9 The 1.3- μm -infrared photocurrent enhancement vs. mechanical strain.

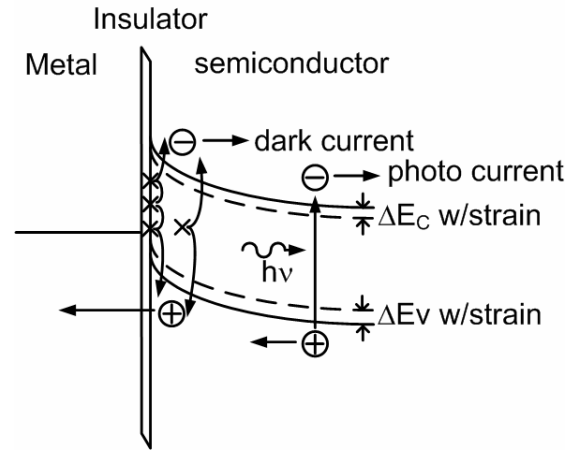


Fig. 10 The band diagram of MIS detector at inversion bias. The external mechanical strain results in bandgap narrowing.

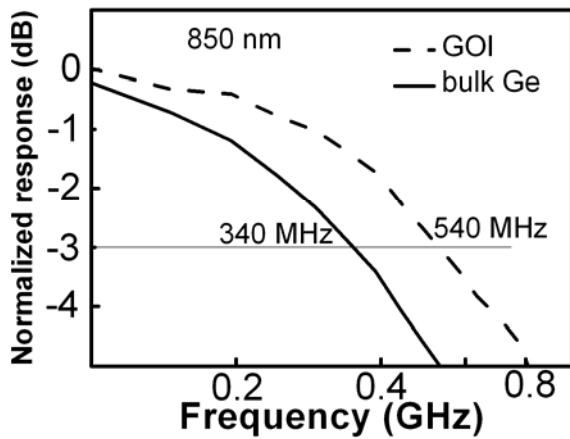


Fig. 11 The 850 nm transient response measurement of the GOI and the bulk Ge detector. The GOI detector shows 60 % enhancement of speed as compared to the bulk Ge detector.

Visible light detection

A single crystalline thin film of Ge on glass (GOG) is also fabricated using wafer bonding and smart cut. The Corning 7059 glass was prepared as a handle wafer instead of the p-Si with thermal oxide as mentioned above. The handle wafer was then hydrophilically cleaned in the $\text{NH}_4\text{OH} : \text{H}_2\text{O}_2 : \text{H}_2\text{O}$ (SC1) solution. The glass substrate is transparent for the visible light, and the GOG MIS photodetectors can be used for the system-on-panel applications.

The GOG structure can be etched before the fabrication of the MIS photodetector to reduce the surface roughness and to remove most defects formed during the implantation process. The surface roughness of the GOG structure was ~ 14 nm after smart-cut. The SC1 solution ($\text{NH}_4\text{OH} : \text{H}_2\text{O}_2 : \text{H}_2\text{O} = 1 : 1 : 7$) is used to etch the Ge in order to remove the defective hydrogen implantation region [12]. The surface roughness decreases to ~ 4 nm after etching for 150 seconds.

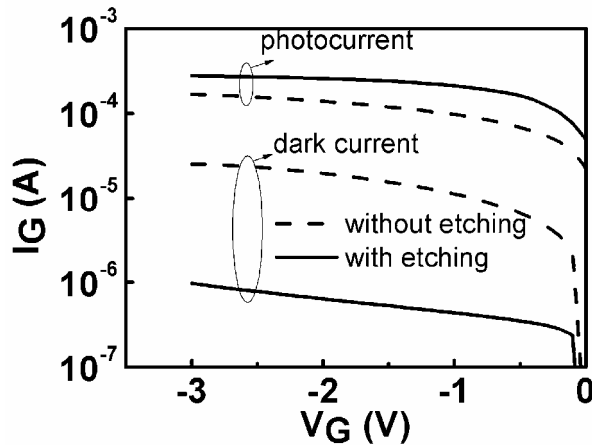


Fig. 12 The dark currents and 532 nm photocurrents of the unetched and etched GOG MIS photodetectors. The power of light source is 4.2 mW.

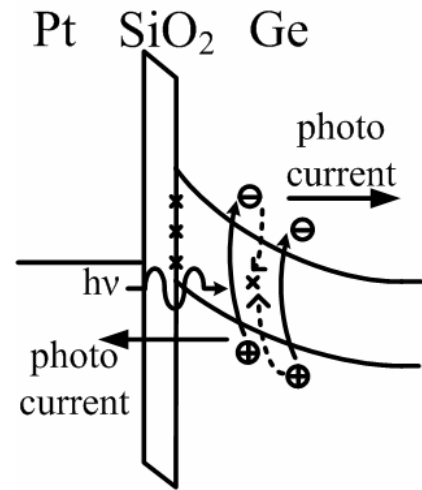


Fig. 13 The mechanism of the photocurrent formation. Photo-generated electrons and holes may recombine via defects without forming the photocurrent.

The GOG structure can be etched to remove most defects formed during the implantation process. Fig. 12 shows the dark currents and photocurrents at 532 nm wavelength of the unetched and etched GOG MIS photodetectors. The dark current of the etched GOG MIS photodetector is reduced by a factor of 30, while the 532 nm photocurrent is increased by a factor of 1.85. The thermal generated electron-hole pairs via defects at the Ge/SiO₂ interface and in the depletion region of Ge decrease after the damage removal, and the dark current consequently decreases. The photo-generated electron-hole pairs should be swept separately

to contribute to the photocurrent. However, these photo-generated electrons and holes may recombine via defects without forming the photocurrent (Fig. 13). The defect density decreases after the etching process, and the recombination of photo-generated carriers is significantly suppressed. This phenomenon is especially significant for visible light detection. The etched devices can enhance the responsivity as long as the remaining Ge layer is sufficiently thicker than absorption depth at exposure wavelength. This is true for 532 nm and 635 nm wavelength which have absorption depth of ~ 20 nm and ~ 50 nm, respectively, in Ge. Note that the remaining Ge after etching is ~ 770 nm. The responsivities of the etched detector for red- and green- light are 0.093 A/W and 0.061 A/W, respectively (Fig. 14).

The responsivities at 1.3 μm and 1.55 μm infrared of the unetched GOG MIS photodetector are 0.27 A/W and 0.05 A/W, respectively, which are larger than those of the etched GOG MIS photodetector. The drop of responsivity at 1.3 μm and 1.55 μm wavelength after etching is due to the insufficient Ge layer thickness (770 nm) as compared to absorption depth of 1.3 μm and 22 μm [13], respectively. Note that there was no Anti Reflection (AR) coating used on the detectors. The further enhancement on responsivity can be expected with the AR coating.

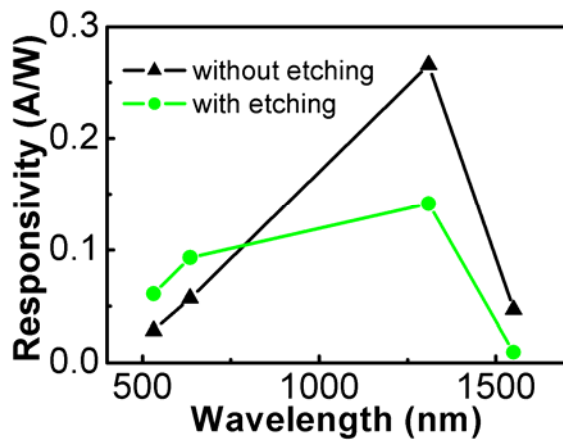


Fig. 14 The responsivities of etched and unetched GOG MIS photodetectors at visible light and telecommunication wavelength.

Summary

The GOI MIS detectors have been demonstrated, and the process temperature is as low as 150°C. The implantation induced defects were effectively passivated by hydrogen ions at low-temperature process, and the degradation of responsivity due to the defects can be suppressed. The MIS detector can have a lower dark current and a simple process without n and p dopant implantation or diffusion. Due to the compatibility with Si ultra-large scale integration, it is possible to integrate electro-optical devices into Si chip for optical communication at the wavelength of 850 nm, 1.3 μm and 1.55 μm . With the external mechanical strain, the photocurrent enhancement can reach 11 %, while the dark current

variation is smaller than 2 %. The red- and green- responses have been measured, and are 0.093 A/W and 0.061 A/W, respectively. The etching is proven to be an effective method to remove implantation damage. After the damage removal, the dark currents can be decreased and the responsivities can be increased while the remaining Ge is sufficiently thick as compared to absorption depth.

REFERENCES

- [1] Sebastian M. Csutak, Jeremy D. Schaub, Wei E. Wu, Rob Shimer, and Joe C. Campbell, "CMOS-Compatible High-Speed Planar Silicon Photodiodes Fabricated on SOI Substrates" *IEEE J. Quantum Electron.*, vol. 38, no.2, pp.193- 196, Feb. 2002.
- [2] G. Dehlinger, S. J. Koester, J. D. Schaub, J. O. Chu, Q. C. Ouyang, and A. Grill, "High-Speed Germanium-on-SOI Lateral PIN Photodiodes" *IEEE Photon. Technol. Lett.*, vol. 16, no. 11, pp. 2547-2549, Nov. 2004.
- [3] E. Kasper, M. Oehme, J. Werner, M. Jutzi and M. Berroth, "Fast Ge p-i-n photodetectors on Si" in *Proc. International SiGe Technology and Device Meeting (ISTDM)*, Princeton, NJ, 2006, pp. 38-39.
- [4] Frank Fournel, Hubert Moriceau, Bernard Aspar, Karine Rousseau, Joel Eymery, Jean-Luc Rouviere, and Noel Magnea, "Accurate control of the misorientation angles in direct wafer bonding" *Appl. Phys. Lett.*, vol. 80, no. 5, pp. 793-795, Feb. 2002.
- [5] S. M. Sze, *Physics of Semiconductor Devices* (2nd Edition). Taipei, Taiwan, R.O.C., 1985, p. 304.
- [6] B.-C. Hsu, S. T. Chang, T.-C. Chen, P.-S. Kuo, P. S. Chen, Z. Pei, and C. W. Liu, "A High efficient 820 nm MOS Ge Quantum Dot Photodetector" *IEEE Electron Device Lett.*, vol. 24, no. 5, pp. 318-320, May 2003.
- [7] O. Madelung, *Data in Science and Technology, Semiconductors* (Springer, New York, 1991).
- [8] C.-H. Lin, B.-C. Hsu, M. H. Lee, and C. W. Liu, "A comprehensive study of gate inversion current of metal-oxide-silicon tunneling diodes," *IEEE Trans. Electron Devices*, vol. 48, no. 9, pp. 2125-2130, Sept. 2001.
- [9] S. M. Sze, *Physics of Semiconductor Devices*, 2nd Ed. (Wiley, New York, 1985), p. 254.
- [10] L. Colace, G. Masini, and G. Assanto, "Ge-on-Si Approaches to the Detection of Near-Infrared Light," *IEEE J. Qunatum Electron.*, vol. 35, no. 12, pp. 1843-1852, Dec. 1999.
- [11] M. H. Liao, P.-S. Kuo, S.-R. Jan, S.-T. Chang, C. W. Liu, "Strained Pt Schottky diodes on n-type Si and Ge," *Appl. Phys. Lett.*, vol. 88, no. 14, p. 143509, Apr. 2006.
- [12] M. Heyns, M. Meuris, and M. Caymax, "Ge and III/V as enabling materials for future CMOS technologies," *ECS Transactions*, vol. 3, no. 7, p. 511, Oct. 2006.
- [13] O. I. Dosunmu, D. D. Cannon, M. K. Emsley, B. Ghyselen, J. Liu, L. C. Kimerling, and M. S. Unlu "Resonant Cavity Enhanced Ge Photodetectors for 1550 nm Operation on Reflecting Si Substrates," *IEEE J. Select. Topics Quantum Electron.*, vol. 10, no. 4, pp. 694-701, Jul. 2004.

Publication supported by this project: REFEREED JOURNAL PAPER

1. C.-H. Lin, C.-Y. Yu, C.-Y. Peng, W. S. Ho, and **C. W. Liu**, "Broadband SiGe/Si quantum dot infrared photodetectors," *J. Appl. Phys.*, Vol. 101, 033117, 2007.
2. M. H. Liao, P.-S. Kuo, S.-R. Jan, S.-T. Chang, **C. W. Liu**, "Strained Pt Schottky diodes on n-type Si and Ge," *Appl. Phys. Lett.*, Vol. 88, 143509, 2006.
3. C.-H. Lin, C.-Y. Yu, P.-S. Kuo, C.-C. Chang, T.-H. Guo, and **C. W. Liu**, " δ -doped MOS Ge/Si quantum dot/well infrared photodetector," *Thin Solid Films*, Vol. 508, 389, 2006.
4. C.-Y. Yu, C.-Y. Lee, C.-H. Lin, and **C. W. Liu**, "Low-temperature fabrication and characterization of Ge-on-Insulator structures," *Appl. Phys. Lett.* Vol. 89, 101913, 2006.

REFEREED INTERNATIONAL CONFERENCE PAPERS

1. C.-H. Lin, C.-Y. Yu, M. H. Liao, C.-F. Huang, C.-J. Lee, C.-Y. Lee, and C. W. Liu, "The Process and Optoelectronic Characterization of Ge-on-Insulator", *210 Meeting of ECS*, Mexico, Oct. 29-Nov. 3, 2006, and *ECS Transactions – Cancun*, vol. 3.

Broadband SiGe/Si quantum dot infrared photodetectors

C.-H. Lin, C.-Y. Yu, C.-Y. Peng, W. S. Ho, and C. W. Liu^{a)}

Department of Electrical Engineering, National Taiwan University, Taipei, Taiwan 106, Republic of China and Graduate Institute of Electronics Engineering, National Taiwan University, Taipei, Taiwan 106, Republic of China

(Received 26 August 2006; accepted 30 November 2006; published online 12 February 2007)

The broadband absorption of metal-oxide-semiconductor SiGe/Si quantum dot infrared photodetectors is demonstrated using boron δ doping in the Si spacer. The peak at 3.7–6 μm results from the intersubband transition in the SiGe quantum dot layers. The other peak at 6–16 μm mainly comes from the intraband transition in the boron δ -doping wells in the Si spacers. Since the atmospheric transmission windows are located at 3–5.3 and 7.5–14 μm , broadband detection is feasible using this device. The δ doping in SiGe quantum dots and $\text{Si}_{0.9}\text{Ge}_{0.1}$ quantum wells is also investigated to identify the origin of the absorption. © 2007 American Institute of Physics. [DOI: 10.1063/1.2433768]

I. INTRODUCTION

Broadband infrared detection is attractive in thermal imaging, target identification, medical, and other applications.¹ Broadband photodetectors demonstrated so far are based on III-V materials.^{2,3} With the advantages of integration with Si electronics and low cost,⁴ the Si-based broadband detectors are highly desirable.

A quantum dot infrared photodetector (QDIP) provides the advantages of no polarization selection rule (normal incident), small dark current, and high operation temperature. Due to the Stranski-Krastanov growth mode of quantum dots (QDs), the size of dots and width of wetting layers are hardly changed. As a result, the absorption region is limited to a certain wavelength. Quantum wells (QWs) with different thickness or compositions can be fabricated to achieve multicolor detection.⁵ However, strain due to the misfit between Ge and Si has to be considered to avoid the formation of dislocations.

We present a metal-oxide-semiconductor (MOS) SiGe/Si QDIP with δ doping in the Si spacer, with a broadband spectrum covering most of the 3–5.3 and 7.5–14 μm atmospheric transmission windows. The δ doping in Si spacers provides the QDs with a sufficient hole concentration and forms a δ -doping well in Si. Due to the strong electric field formed by locally ionized dopants and band gap narrowing by delocalization of acceptor states in the reciprocal space, a QW is formed in the valence band of Si spacers.⁶ The holes in QDs could be excited by mid-wavelength infrared (3.7–6 μm detection). The δ -doping QWs contribute to long-wavelength infrared detection through intraband transition (cutoff wavelength at 16 μm). Boron δ doping in QDIPs achieves broadband detection without increasing the process complexity, as compared with the complex process to incorporate SiGe QWs.

The MOS structure uses an ultrathin tunneling oxide to allow carrier tunneling under infrared excitation and to re-

duce dark current. This simple structure of the MOS detector is attractive for integration with Si electronics. Note that the detector should be operated in the inversion bias region to reduce dark current.

II. DEVICE FABRICATION

The 20-period SiGe QDs with a 2–3 nm wetting layer were grown on 100 mm *p*-type (100) Si substrates with the resistivity of 15–25 $\Omega\text{ cm}$ by ultrahigh vacuum chemical vapor deposition (UHV-CVD). Due to different *in situ* annealing times and interdiffusion between Si and Ge, the top SiGe dot with shorter annealing time after formation has a higher Ge concentration ($\sim 60\%$) as compared to the bottom SiGe dot ($\sim 40\%$),^{7,8} which suffers longer annealing time after formation. The different Ge concentrations are due to the difference in thermal budget after growth. The Ge concentration variation reflects the broad peaks in photoluminescence and absorption measurements. A 2 nm layer of low-temperature (50 $^{\circ}\text{C}$) oxide⁹ was deposited on top of the sample by liquid phase deposition (LPD) to fabricate MOS tunneling diodes¹⁰ (Fig. 1). SiGe QD layers were separated by 80 nm Si spacer layers. Boron (10^{19} cm^{-3}) was δ introduced in the middle of the growth of each Si spacer layer. Al was deposited on top of the oxide to form the gate electrode (with an area of $3 \times 10^{-2}\text{ cm}^2$), and also deposited on the back of the sample to form the Ohmic contact.

The large valence band offset between Si and SiGe forms discrete quantum states in the SiGe QDs. Under infrared exposure, the confined holes can be excited and contribute to the photocurrent. The spectral response is measured by a Fourier transform infrared (FTIR) spectrometer (Perkin-Elmer Spectrum 2000) coupled with a cryostat and an SR570 current preamplifier. The incident light is unpolarized and the devices are under normal incidence.

To further study the absorption mechanism, two other samples with the same δ -doping profile are also measured for comparison (Table I). The “ δ -spacer” and “ δ -QD” samples have the same QD structure, but with different δ -doping locations. The former is in the Si spacer, while the latter is in

^{a)} Author to whom correspondence should be addressed; electronic mail: chee@cc.ee.ntu.edu.tw

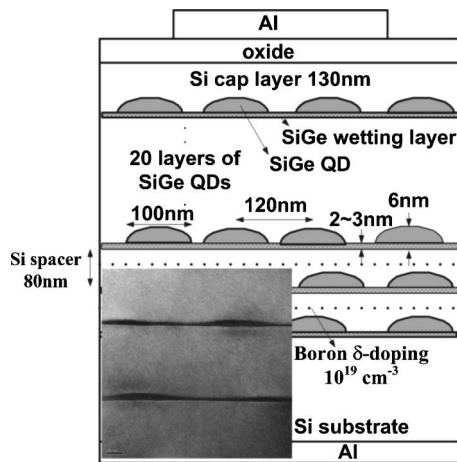


FIG. 1. The structure of the MOS SiGe/Si QDIP. The 20-layer SiGe quantum dots were formed by ultrahigh vacuum chemical vapor deposition, and the δ doping was introduced in the Si spacer. The inset shows the TEM photograph of SiGe quantum dots.

the SiGe QD layer. The “ δ -SiGe01” sample has five-period 7-nm-thick $\text{Si}_{0.9}\text{Ge}_{0.1}$ quantum wells with the boron δ doping in quantum wells.

III. RESULTS AND DISCUSSION

At 15 K, the absorption spectra can be grouped into three regions, including a 1.8–2.37 μm peak (the inset of Fig. 2), a 3.7–6 μm peak, and a 6–16 μm peak (Fig. 2). The schematic energy levels in Si/SiGe/Si QDs are shown in Fig. 3.

The 1.8–2.37 μm peak results from the intervalence band transition (E_1 in Fig. 3) between heavy hole ground

TABLE I. Condition of three different samples.

Sample name	Active layer	δ -doping location	Spacer width (nm)	Cap thickness (nm)
δ -spacer	20 layers SiGe QD	Spacer	80	130
δ -QD	20 layers SiGe QD	QD	80	130
δ -SiGe01	5 layers $\text{Si}_{0.9}\text{Ge}_{0.1}$ QW	QW	90	135

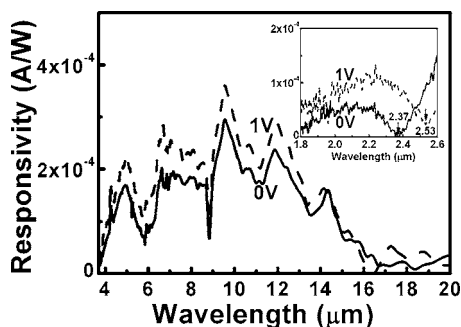


FIG. 2. Spectral response of the δ -spacer sample at 0 and 1 V (15 K). The inset shows the response at shorter wavelength, indicating cutoff wavelength at 2.37 μm at 0 V and 2.53 μm at 1 V.

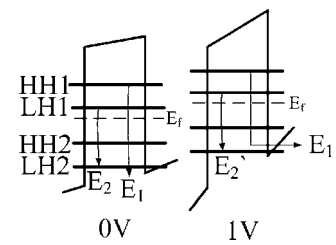


FIG. 3. The schematic energy levels in Si/SiGe/Si quantum dots under different biases. The band is not flat at 0 V since the flatband voltage is negative.

state (HH1) and the continuum states. When the applied voltage increases from 0 to 1 V, the cutoff wavelength shifts from 2.37 μm (0.52 eV) to 2.53 μm (0.49 eV) (the inset of Fig. 2). Holes, which are excited by photons with energy less than the energy difference between the ground state and the barrier, can tunnel through the triangular barrier at 1 V (Fig. 3). The redshift is characteristic of bound-to-continuum transition.^{11,12}

The photoluminescence (PL) spectrum at 10 K is shown in Fig. 4. Since the conduction band offset at the Si/SiGe heterojunction is very small and the ground state (HH1) is very close to the valence band edge of SiGe dots, the HH1-to-continuum transition energy approximately coincides with the energy gap difference between Si (1.17 eV) and SiGe dots (0.7 eV).

The hole concentration of light hole ground state (LH1) is smaller than that of HH1. The LH1-to-continuum transition should be much weaker than the HH1-to-continuum transition, and no obvious absorption is observed.

The 3.7–6 μm peak results from the intersubband transition (E_2 in Fig. 3) between the ground state of light hole (LH1) and the first excited state of light hole (LH2) in the SiGe-dot layers. The 3.7–6 μm peak does not shift as the gate voltage increases, since the LH1-to-LH2 transition (3.7–6 μm peak) occurs between two bound states, and the influence of a triangular barrier is small.

The continuous supply of holes to the SiGe/Si QDs is necessary when the photogenerated holes are collected by the electrode at the bottom of the substrates (Fig. 5). Two possible mechanisms could be responsible for the supply of holes. One is the electron-hole pair generation at oxide/semiconductor interface. The electrons in the valence band jump into the conduction band via interface states, and tunnel into the gate electrode through the thin oxide (2 nm), and

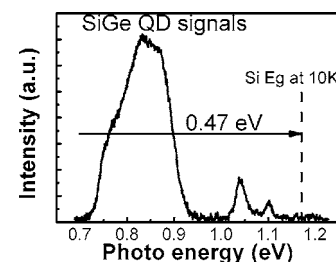


FIG. 4. The photoluminescence (PL) spectrum of the δ -spacer sample at 10 K. The band edge of the SiGe dot signal corresponding to HH1 to conduction band in SiGe dot is ~ 0.7 eV.

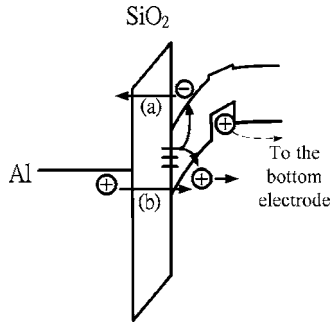


FIG. 5. Two possible mechanisms responsible for the hole supply. (a) Electrons in the valence band jump into the conduction band via interface states and tunnel into the gate electrode through the thin oxide, and the holes are left in the valence band. (b) Holes tunnel from the gate electrode to Si.

the holes are left in the valence band. The other mechanism is that holes tunnel from the gate electrode to Si.

The 6–16 μm peak mainly comes from the intraband (intersubband or intervalence band) transition in the boron δ -doping wells in the Si spacers. For the shorter wavelength part in the 6–16 μm peak (about 6–10 μm), there are other possible transitions in QDs such as the intersubband transition from HH1 to HH2 and the intervalence band transition from HH1 to LH1. However, the excited states (HH2 and LH1) are far from the top of the barrier, preventing photoexcited carriers to be efficiently collected.¹³ Therefore, the transitions (HH1 to HH2 and HH1 to LH1) may have a small contribution to the 6–10 μm absorption. Moreover, oxygen with an impurity level of 160 meV (7.8 μm) may also contribute to the 6–10 μm absorption.¹⁴

For comparison, the infrared spectra of the three samples in Table I are shown in Fig. 6. The cutoff wavelengths of δ -spacer and δ -SiGe01 samples at the low energy end are 16 and 14 μm , respectively. These transitions result from the intraband transition of δ -doping well (Fig. 7). The blueshift of the cutoff wavelength of the δ -SiGe01 sample as compared with the δ -spacer sample is probably due to the additional quantum confinement of Si_{0.9}Ge_{0.1} QW outside the δ -doping well. Note that there is a valence band offset of ~ 75 meV between Si and Si_{0.9}Ge_{0.1}. The long-wavelength (< 14 μm) transition in the δ -SiGe01 sample cannot originate from intraband transition of Si_{0.9}Ge_{0.1} QW due to the

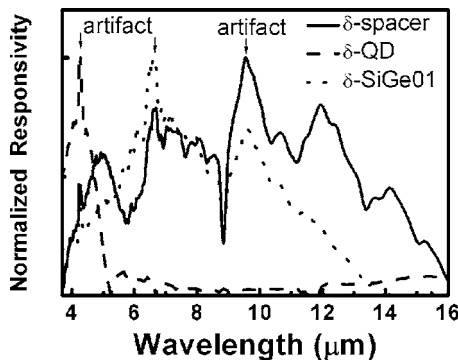


FIG. 6. Comparison of the spectral responses of the δ -spacer sample, the δ -QD sample, and the δ -SiGe01 sample at 15 K (at 1 V bias). Both the δ -spacer sample and the δ -SiGe01 sample have a long-wavelength transition.

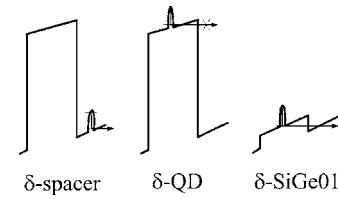


FIG. 7. The schematic detection of long-wavelength infrared inside the δ -doping layer. The long-wavelength infrared photoexcited carriers can be collected in the δ -spacer sample and δ -SiGe01 sample. No absorption around 6–16 μm is observed in the δ -QD sample, since the valence band barrier of SiGe QD is too large to block the photoexcited hole from the δ -doping well.

QW's shallow depth, where the cutoff wavelength should be larger than 16.5 μm (75 meV). No absorption around 6–16 μm is observed in the δ -QD sample. Since the valence band barrier of SiGe QD is large enough to block the photoexcited holes from the δ -doping well, the photoexcited carriers cannot be collected by the electrode (Fig. 7).

For the intersubband transition from LH1 to LH2, the cutoff wavelengths of the δ -QD sample and the δ -spacer sample are 5 and 6 μm , respectively. The smaller cutoff wavelength of the δ -QD sample may be due to the many body effect, since the hole concentration in the QDs is higher. The many body effect increases the intersubband transition energy.^{15,16}

Note that there are some artifacts, such as 2.6, 4.3, 6.6, and 9.5 μm (Fig. 6), due to the absorption from the measurement environment.

The normalized detectivity D^* is

$$D^* = \frac{\sqrt{A\Delta f}}{NEP} = \frac{\sqrt{A\Delta f}}{i_n/R}, \quad (1)$$

where A is the detector area ($3 \times 10^{-2} \text{ cm}^2$) and Δf is the equivalent bandwidth of the electronic system. The noise equivalent power is defined as i_n/R , where i_n is the current noise and R is the responsivity. At 1 V, the current noise is limited by the dark current and can be approximated as the shot noise $(2eI_d\Delta f)^{1/2}$, where I_d is the measured dark current. At 0 V, the dark current approaches zero, and the current noise should be approximated as Johnson noise $(4kTG\Delta f)^{1/2}$, where G is the measured conductance.

Therefore, D^* can be simplified as

$$D^* = \frac{\sqrt{AR}}{\sqrt{2eI_d}} \quad \text{at 1 V}, \quad (2)$$

$$D^* = \frac{\sqrt{AR}}{\sqrt{4kTG}} \quad \text{at 0 V}. \quad (3)$$

Figure 8 shows the detectivity at 1 and 0 V bias at different temperatures. At 15 K and 1 V bias, the peak detectivity is found to be $4.3 \times 10^8 \text{ cm Hz}^{1/2}/\text{W}$ at 9.6 μm and $2.6 \times 10^8 \text{ cm Hz}^{1/2}/\text{W}$ at 4.9 μm . The peak detectivity increases to $3.9 \times 10^9 \text{ cm Hz}^{1/2}/\text{W}$ at 9.6 μm and $2.3 \times 10^9 \text{ cm Hz}^{1/2}/\text{W}$ at 4.9 μm when the bias decreases from 1 to 0 V. Note that the conductance measured at 15 K is $2 \times 10^{-7} \text{ S}$. The detectivity decreases as operating temperature increases. The values of detectivity are very low in compari-

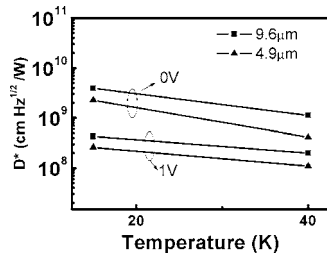


FIG. 8. The detectivity of the δ -spacer sample at different temperatures. The 3.7–6 μm detection has a peak at 4.9 μm , and the 6–16 μm detection has a peak at 9.6 μm .

son with that of commercialized detectors. Further optimization should be done for higher detectivity. Dark current reduction and responsivity enhancement may be the effective steps to improve the detectivity. The dark current could be reduced with a passivation technique to decrease the interface states at Si/LPD SiO_2 interface. Antireflection coating could be used in order to increase the responsivity.

Under negative bias, the electrons in Al gate tunnel to the semiconductor, and this large dark current prevents the detector operation at the negative bias (Fig. 9).

IV. CONCLUSIONS

There are three detection regions for the QDIP with δ doping in the Si spacer, including 1.8–2.37, 3.7–6, and 6–16 μm . The 1.8–2.37 μm peak results from the intervalence band transition from HH1 to the continuum states in the SiGe-dot layers. The 3.7–6 μm peak results from the inter-

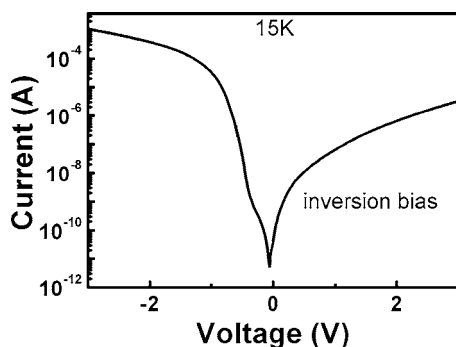


FIG. 9. Dark current of the δ -spacer sample at 15 K. The detector is operated at inversion bias.

subband transition from LH1 to LH2 in the SiGe-dot layers. The cutoff wavelengths of the LH1-to-LH2 transition of the δ -QD and δ -spacer samples are 5 and 6 μm , respectively. The blueshift of the δ -QD sample may be due to the many body effect. The intraband transition in δ -doping quantum wells contributes to long-wavelength infrared detection (6–16 μm). The cutoff wavelengths at the low energy end of δ -spacer and δ -SiGe01 samples are 16 and 14 μm , respectively. The blueshift of the cutoff wavelength of the δ -SiGe01 sample is probably due to the additional quantum confinement of $\text{Si}_{0.9}\text{Ge}_{0.1}$ QW outside the δ -doping well. At 15 K and 0 V, the peak detectivity is found to be $3.9 \times 10^9 \text{ cm Hz}^{1/2}/\text{W}$ for the 6–16 μm peak and $2.3 \times 10^9 \text{ cm Hz}^{1/2}/\text{W}$ for the 3.7–6 μm peak.

ACKNOWLEDGMENTS

This work is supported by the U.S. Air Force Office of Scientific Research/AOARD under Contract No. FA 520904P0441 and the National Science Council, Taiwan, R.O.C. under Contract nos. 95-2221-E-002-357 and 95-2221-E-002-370.

- ¹P. G. Datskos, S. Rajic, L. R. Senesac, and I. Datskou, *Ultramicroscopy* **86**, 191 (2001).
- ²J. Park, S.-J. Jo, S. Hong, and J.-I. Song, *Solid-State Electron.* **46**, 651 (2002).
- ³G. Karunasiri, J. S. Park, J. Chen, R. Shih, J. F. Scheihing, and M. A. Dodd, *Appl. Phys. Lett.* **67**, 2600 (1995).
- ⁴R. People, J. C. Bean, C. G. Bethea, S. K. Sputz, and L. J. Peticolas, *Appl. Phys. Lett.* **61**, 1122 (1992).
- ⁵S. V. Bandara *et al.*, *Appl. Phys. Lett.* **86**, 151104 (2005).
- ⁶J.-h. Zhu, D.-w. Gong, B. Zhang, F. Lu, C. Sheng, H.-h. Sun, and X. Wang, *Phys. Rev. B* **54**, 2662 (1996).
- ⁷M. H. Liao, C.-H. Lin, C.-H. Lee, T.-H. Cheng, T.-H. Guo, and C. W. Liu, ECS Meeting, Cancun, Mexico, No. 1278 (2006).
- ⁸O. G. Schmidt and K. Eberl, *Phys. Rev. B* **61**, 13721 (2000).
- ⁹B.-C. Hsu, S. T. Chang, C.-R. Shie, C.-C. Lai, P. S. Chen, and C. W. Liu, *Tech. Dig. - Int. Electron Devices Meet.* **2002**, 91.
- ¹⁰C. W. Liu, M. H. Lee, C. F. Lin, I. C. Lin, W. T. Liu, and H. H. Lin, *Tech. Dig. - Int. Electron Devices Meet.* **1999**, 749.
- ¹¹B. F. Levine, *J. Appl. Phys.* **74**, R1 (1993).
- ¹²V. D. Jovanovic, P. Harrison, Z. Ikonic, and D. Indjin, *J. Appl. Phys.* **96**, 269 (2004).
- ¹³R. P. G. Karunasiri, J. S. Park, Y. J. Mii, and K. L. Wang, *Appl. Phys. Lett.* **57**, 2585 (1990).
- ¹⁴S. M. Sze, *Physics of Semiconductor Devices*, 2nd ed. (Wiley, New York, 1985), Part 1, p. 21.
- ¹⁵G. Karunasiri, *Jpn. J. Appl. Phys., Part 1* **33**, 2401 (1994).
- ¹⁶Z. Chen, C. M. Hu, P. L. Liu, G. L. Shi, and S. C. Shen, *J. Appl. Phys.* **82**, 3900 (1997).

Strained Pt Schottky diodes on *n*-type Si and Ge

M. H. Liao

Department of Electrical Engineering and Graduate Institute of Electro-Optical Engineering,
National Taiwan University, Taipei, Taiwan, Republic of China

P.-S. Kuo and S.-R. Jan

Department of Electrical Engineering and Graduate Institute of Electronics Engineering,
National Taiwan University, Taipei, Taiwan, Republic of China

S. T. Chang

Department of Electrical Engineering, National Chung Hsing University, Taichung, Taiwan,
Republic of China

C. W. Liu^{a)}

Department of Electrical Engineering, Graduate Institute of Electro-Optical Engineering,
and Graduate Institute of Electronics Engineering, National Taiwan University, Taipei, Taiwan,
Republic of China

(Received 7 November 2005; accepted 16 February 2006; published online 5 April 2006)

The variation of electron barrier height and built-in voltage of Pt Schottky diodes on the mechanically strained *n*-type Si and Ge is investigated experimentally and theoretically. The mechanical strain is measured by Raman spectroscopy and analyzed by the finite element method. The built-in voltage and barrier height measured by capacitance-voltage and current-voltage methods, respectively, decrease with increasing external tensile strain. The reduction of the built-in voltage and barrier height originates mainly from the conduction band lowering with strain. The extracted value of conduction band lowering is consistent with the theoretical calculations using the “stress-free” boundary condition. © 2006 American Institute of Physics. [DOI: 10.1063/1.2191831]

Strained Si and Schottky barrier source/drain technologies have received considerable attention recently and can be used for high performance metal oxide semiconductor field effect transistors (MOSFETs).^{1,2} The substrate strain technology using the lattice misfit between Si and SiGe yields global biaxial strain and changes the conduction band and the valence band structure of Si. The carrier effective mass and the intervalley scattering are reduced, and thus the mobility is enhanced. Process and package induced strains can also produce sufficient strain for mobility enhancement at low cost.^{3,4} Schottky barriers improve the short channel effect due to the shallow junction.² The previous study of the Schottky barrier height on the Pt/*p*-strained Si Schottky diode was reported.⁵ The external biaxial strain to reduce the Schottky barrier height and to increase complementary MOSFET drive current was also calculated by another group.⁶ In this Letter, the effect of externally mechanical strain on *n*-type Schottky barrier diodes on Si and Ge is presented experimentally and theoretically, and the shifts of the conduction band edge with mechanical strain are also studied.

The *n*-Si (100) and *n*-Ge (100) wafers used in this study were cleaned by dipping in dilute HF to remove the native oxide layer just before loading in the deposition chamber. Pt was deposited through a shadow mask with an area of $5 \times 10^{-3} \text{ cm}^2$ by electron beam evaporation at a pressure of 2×10^{-6} mbar to form the Schottky diodes. The Ohmic contact was made by thermal evaporation of Al on the back side of the wafer. The experimental setup to apply external mechanical strain to Schottky barrier diodes is similar to that

described in Refs. 7 and 8. Two external strain conditions are applied in this work: (1) uniaxial tensile strain along the $\langle 110 \rangle$ directions on (001) substrate and (2) biaxial tensile strain on (001) substrate. The level of strain is determined by the four screws on the sides of the washer. The strain of the Si and Ge under mechanical strain is simulated by finite element method (ANSYS) and measured by Raman spectroscopy. Raman spectra were excited by an Ar laser (wavelength of 514 nm). The Ge-Ge peak in the Raman spectra (Fig. 1) shifts towards the negative axis under mechanical tensile strain. The Raman shifts of 0.91 and 1.32 cm^{-1} under uniaxial and biaxial tensile strains, respectively, were extracted from the curve fitting using a Lorentzian profile. The strain is obtained by⁹

$$\Delta\omega = \frac{1}{2\omega_0} [p\varepsilon_{zz} + q(\varepsilon_{xx} + \varepsilon_{yy})]. \quad (1)$$

For biaxial tensile strain,

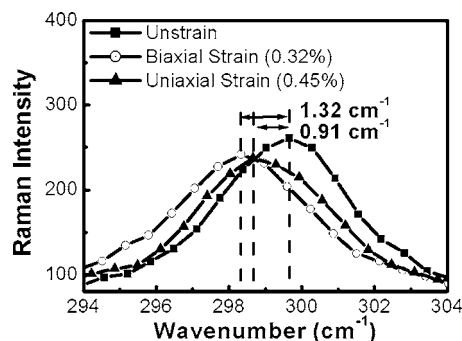


FIG. 1. Raman spectra of the mechanically strained Ge. The position of Ge-Ge peak of strained Ge indicates 0.32% for the biaxial tensile strain and 0.45% for the uniaxial tensile strain.

^{a)} Author to whom correspondence should be addressed; electronic mail: chee@cc.ee.ntu.edu.tw

TABLE I. The numerical value of parameters used in the calculation.

	C_{11} (GPa)	C_{12} (GPa)	C_{44} (GPa)	S_{11} (GPa)	S_{12} (GPa)	S_{44} (GPa)	p (10^{27} s^{-2})	q (10^{27} s^{-2})	$\Xi_d + (1/3)\Xi_u$ (eV)
Si _(Δ)	167	65	79	770	-214	126	-14.3	-18.9	4.18
Ge _(L)	131	49	66	960	-261	151	-4.7	-6.17	-6.84

$$\varepsilon_{zz} = -(2C_{12})/(C_{11})\varepsilon_{xx}, \quad \varepsilon_{xx} = \varepsilon_{yy}. \quad (2)$$

For uniaxial tensile strain,

$$\varepsilon_{xx} = 0.5T(S_{11} + S_{12}) + 0.25TS_{44}, \quad (3)$$

$$\varepsilon_{yy} = 0.5T(S_{11} + S_{12}) - 0.25TS_{44}, \quad (4)$$

$$\varepsilon_{zz} = TS_{12}, \quad (5)$$

where ω_0 is the longitudinal phonon frequency at the zone center of reciprocal space, p and q are phenomenological potentials to calculate the frequency shift as the function of external strain in Raman spectra, ε_{xx} , ε_{yy} , ε_{zz} are the strain along the $\langle 110 \rangle$, $\langle 1\bar{1}0 \rangle$, $\langle 001 \rangle$ directions on (100) wafer, T is the stress, and S_{11} , S_{12} , S_{44} , C_{11} , and C_{12} are elastic coefficients. The material parameters used in the calculation are given in Table I.^{9,10} In Table I, the $\Xi_d + (1/3)\Xi_u$ is the deformation potential constant to calculate the conduction band shift of Si and Ge as a function of external strain. Using the Raman shift of the Ge-Ge phonon peak in Fig. 1, the strain in Ge is estimated to be 0.32% for biaxial strain and 0.45% for uniaxial strain. Similarly, the strain in Si can also be estimated to be 0.13% for biaxial strain and 0.35% for uniaxial strain.⁷ The strain level obtained from Raman shift agrees well with the finite element simulation using ANSYS software.

Figure 2 shows the current-voltage (I - V) characteristic of Pt/ n -Si and Pt/ n -Ge Schottky barrier diodes under biaxial tensile and uniaxial tensile mechanical strains. The barrier height and ideality factor (n) can be calculated from the forward I - V curves. The ideality factors of $n=1.07$ and $n=1.13$ for Si and Ge are observed, respectively, indicating that the current is mainly due to the thermionic emission.¹¹ The barrier height changes of the Pt/ n -Ge sample are found to be -9 and -27 meV for uniaxial strain ($\sim 0.45\%$) and biaxial strain ($\sim 0.32\%$), respectively. For Pt/ n -Si diode, the changes are -8 and -13 meV for uniaxial strain ($\sim 0.35\%$) and biaxial strain ($\sim 0.13\%$), respectively. The Schottky barrier height decreases with increase of external mechanical

tensile strain. Neglecting the effect of surface dipole, the barrier height change of a Schottky junction under mechanical strain can be written as

$$\Delta\phi_{bn}(\varepsilon) = \Delta\phi_m(\varepsilon) - \Delta\chi(\varepsilon), \quad (6)$$

where ϕ_{bn} , ϕ_m , and χ represent barrier height, metal work function, and electron affinity of the semiconductor, respectively. The change of metal work function $\phi_m(\varepsilon)$ for single crystalline Pt is within ~ 4 meV under our mechanical strain conditions based on the derivation in Ref. 12.

$$\frac{E_{F,\text{strain}}}{E_{F,\text{unstrain}}} = \left(\frac{V_{\text{unstrain}}}{V_{\text{strain}}} \right)^{2/3}, \quad (7)$$

where V is the volume of metal and E_F is the Fermi energy. Since the Pt in our sample is polycrystalline, the exact strain in the polygrains can be even smaller, and the change of the work function can be neglected. Therefore, the change of the Schottky barrier height under mechanical strain is mainly due to the change of the conduction band edge of the semiconductor.

Capacitance-voltage (C - V) characteristics of Pt/ n -Si and Pt/ n -Ge samples under the biaxial tensile or uniaxial tensile strain are shown in Fig. 3. The doping concentrations obtained from the Si and Ge devices at reverse bias are $\sim 1 \times 10^{15}$ and $\sim 1 \times 10^{16} \text{ cm}^{-3}$, respectively. The barrier height variation can be determined from¹¹

$$\Delta\phi_{bn}(\varepsilon) = \Delta V_{bi}(\varepsilon) + \Delta(E_C - E_F)(\varepsilon), \quad (8)$$

where $V_{bi}(\varepsilon)$ is the built-in voltage measured from the voltage intercept of C - V , and $(E_C - E_F)(\varepsilon)$ is the depth of the Fermi level below the conduction band, which can be computed when the doping concentration is known,

$$\Delta(E_C - E_F)(\varepsilon) = -KT \ln \left[\frac{n}{N_c(\varepsilon)} \right], \quad (9)$$

where $N_c(\varepsilon)$ is the electron effective density of state as a function of strain in Si and Ge, respectively.¹³ Based on C - V measurement, the barrier height also decreases with external tensile strain.

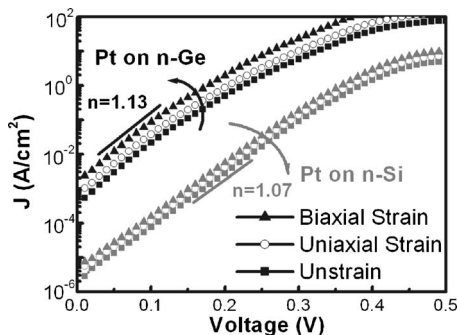


FIG. 2. Experimental forward I - V characteristics of Pt/ n -Si and Pt/ n -Ge Schottky diodes with and without mechanical strain.

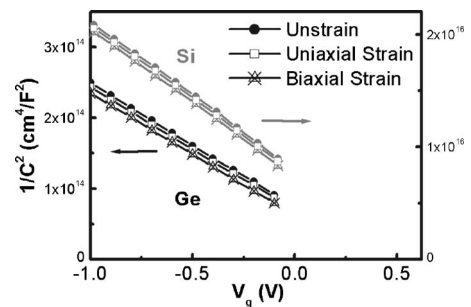


FIG. 3. C - V characteristic of Pt/ n -Si and Pt/ n -Ge Schottky diodes with and without mechanical strain.

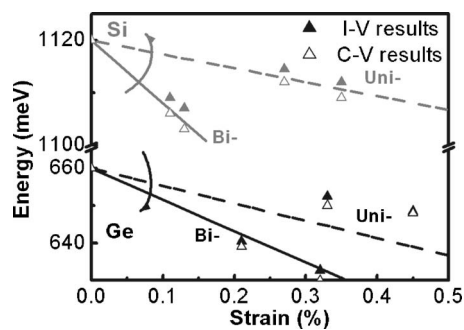


FIG. 4. Theoretical calculation and the experimental data of the shift of conduction band of Si and Ge under the external mechanical strain.

The theoretical calculation and experimental data of the conduction band shift in Si and Ge as a function of external strain along $\langle 110 \rangle$ are shown in Fig. 4. Using the parameters in Refs. 10 and 14, and the formulas in Refs. 14 and 15, the shift of conduction band edge due to external tensile strain along $\langle 110 \rangle$ is calculated under the stress-free condition. "Stress-free" means no stress along the in-plane direction perpendicular to the uniaxial strain axis $\langle 110 \rangle$, i.e., $\langle 1\bar{1}0 \rangle$ direction. The downshifts of -23 (-22) meV/% for the uniaxial strain and -100 (-84) meV/% for the biaxial strain are obtained for the Si (Ge) devices from I - V measurement.

In summary, the reduction of the Schottky barrier height for the n -type semiconductor under external mechanical strain is observed. This reduction is shown to originate from the reduction of the conduction band edge. Using the stress-free boundary condition, a reasonable agreement between experimental data and theoretical calculation is obtained.

Raman measurements by Professor Chih-Ta Chia at the National Taiwan Normal University is highly appreciated. This work is supported by the National Science Council of ROC under Contract Nos. 94-2215-E-002-040 and 94-2215-E-002-041, and the Asian Office of Aerospace Research and Development (AOARD), US Air Force.

- ¹C. W. Liu, S. Maikap, and C.-Y. Yu, IEEE Circuits Devices Mag. **21**, 21 (2005).
- ²M. Fritze, C. L. Chen, S. Calawa, D. Yost, B. Wheeler, P. Wyatt, C. L. Keast, J. Snyder, and J. Larson, IEEE Electron Device Lett. **25**, 220 (2004).
- ³F. Yuan, C.-F. Huang, M.-H. Yu, and C. W. Liu, IEEE Trans. Electron Devices **53**, 724 (2006).
- ⁴M. H. Liao, S. T. Chang, M. H. Lee, S. Maikap, and C. W. Liu, J. Appl. Phys. **98**, 066104 (2005).
- ⁵S. Chattopadhyay, L. K. Bera, S. K. Ray, and C. K. Maiti, Appl. Phys. Lett. **71**, 942 (1997).
- ⁶A. Yagishita, T.-J. King, and J. Bokor, Jpn. J. Appl. Phys., Part 1 **43**, 1713 (2004).
- ⁷M. H. Liao, M.-J. Chen, T. C. Chen, P.-L. Wang, and C. W. Liu, Appl. Phys. Lett. **86**, 223502 (2005).
- ⁸M. H. Liao, C.-Y. Yu, C.-F. Huang, C.-H. Lin, C.-J. Lee, M.-H. Yu, S. T. Chang, C.-Y. Lee, T.-H. Guo, C.-C. Chang, and C. W. Liu, Tech. Dig. - Int. Electron Devices Meet. **1023** (2006).
- ⁹Y. Hida, T. Tamagawa, H. Ueba, and C. Tatsuyama, J. Appl. Phys. **67**, 7274 (1990).
- ¹⁰Properties of Crystalline Silicon, EMIS Data Reviews Series No. 20, edited by R. Hull (INSPEC, London, 1999).
- ¹¹S. M. Sze, Physics of Semiconductor Devices (Wiley, New York, 1981).
- ¹²N. W. Ashcroft and N. D. Mermin, Solid State Physics (Harcourt Brace Jovanovitch, San Diego, 1975), pp. 32-38.
- ¹³M. V. Fischetti and S. E. Laux, J. Appl. Phys. **80**, 2234 (1996).
- ¹⁴C. Ohler, C. Daniels, A. Forster, and H. Luth, Phys. Rev. B **58**, 7864 (1998).
- ¹⁵J.-S. Lim, S. E. Thompson, and J. G. Fossum, IEEE Electron Device Lett. **25**, 731 (2004).

δ -Doped MOS Ge/Si quantum dot/well infrared photodetector

C.-H. Lin^a, C.-Y. Yu^a, P.-S. Kuo^a, C.-C. Chang^a, T.-H. Guo^a, C.W. Liu^{a,b,*}

^a Department of Electrical Engineering and Graduate Institute of Electronics Engineering, National Taiwan University, Taipei, Taiwan, ROC

^b ERSO/ITRI, Hsinchu, Taiwan, ROC

Available online 28 November 2005

Abstract

Metal-oxide-semiconductor tunneling diodes can be used as photodetectors at the inversion bias. To increase the responsivity, δ -doping is used in the quantum dot infrared photodetectors (QDIPs) and quantum well infrared detectors (QWIPs). The peak responsivity of the quantum dot and quantum well infrared photodetector at 15 K is found to be 0.03 mA/W and 1.3 mA/W, respectively, at a gate voltage of 1 V. The higher responsivity of the QWIP is probably due to the continuous two-dimensional density of states and smaller transition energy as compared to the QDIP. The QD photoresponse in the peak wavelength range 3.5–5 μ m can be measured up to 100 K, while that for QW 3–7 μ m can only be detected up to 60 K. A higher dark current due to the lower transition energy in the QWIP limits its operating temperature as compared to the QDIP.

© 2005 Elsevier B.V. All rights reserved.

Keywords: MOS; Silicon; Germanium

1. Introduction

Advanced Si-heterostructure technology can increase the functionality of Si chips with potential applications in optoelectronic devices [1–4]. An ultra-thin insulator in metal–insulator–semiconductor (MIS) structure allows a significant tunneling gate current, which can be used in the photodetectors. Note that a large gate current is not desired in ultra-large scale integration circuit applications.

Mid- and long-wavelength quantum dot/well infrared photodetectors using intraband transitions are attractive in the military, medical, astronomical and other applications [5]. Due to the requirement of a precise control of heterojunction abruptness, most quantum dot/well infrared photodetectors (QDIPs/QWIPs) are grown by Molecular Beam Epitaxy (MBE). In this paper, we have successfully fabricated QDIPs/QWIPs with good performances by Ultrahigh Vacuum Chemical Vapor Deposition (UHVCVD). Schematic structure is shown in Fig. 1.

2. δ -doped quantum dot infrared photodetector

A MOS structure at the inversion bias can significantly reduce the dark current due to the tunneling oxide. Fig. 2 shows that a 5-period of Ge/Si quantum dot infrared photodetector (QDIP) in metal-semiconductor (MS) structure has larger dark current than that in metal-oxide-semiconductor (MOS) structure without δ -doping introduced. The hole excited by an infrared exposure in Ge/Si quantum dots (quantum wells) can transport into the back electrode by relaxation in the p-type semiconductor (the inset of Fig. 3). The δ -doping in the quantum dots (quantum wells) can increase the responsivity due to the increase of hole concentration inside the dots (wells). The valence band offset between Si and Ge (SiGe) forms discrete quantum states in the Ge quantum dots and two-dimensional density of state in the Si_{0.7}Ge_{0.3} quantum wells [6]. The hole transition energy is determined by the band structure of the quantum dots (quantum wells).

A 20-period Ge/Si quantum dots (QDs) with 3 nm wetting layer grown by UHVCVD was fabricated into MOS tunneling diodes [7] with a low-temperature (50 °C) liquid phase deposition (LPD) oxide (Fig. 1) [8]. A boron concentration of 10¹⁹ cm^{−3} was introduced during the growth of Ge quantum dots. Boron incorporation occurred only for the middle one-tenth of deposition time of the Ge layer. Ge quantum dot layers

* Corresponding author. Department of Electrical Engineering and Graduate Institute of Electronics Engineering, National Taiwan University, Taipei, Taiwan, ROC. Tel.: +886 2 23635251x515; fax: +886 2 23638247.

E-mail address: chee@cc.ee.ntu.edu.tw (C.W. Liu).

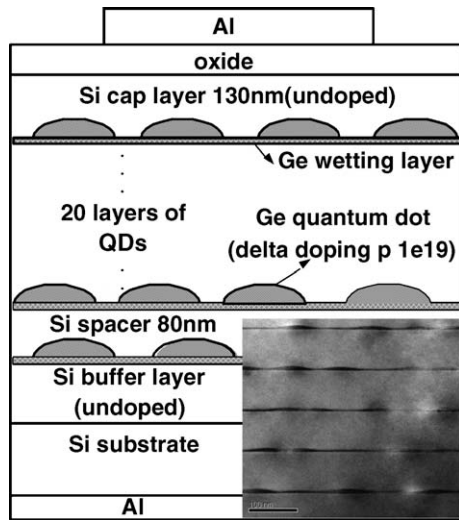


Fig. 1. The structure of MOS Ge/Si QDIP. Twenty-layer Ge quantum dots with δ -doping were prepared by UHVCVD. The inset shows the TEM photograph of the quantum dot structure. The Si spacer is 80 nm in thickness.

were separated by 80 nm Si spacer layer. The cross-sectional TEM photograph of the QD structure is shown in the inset of Fig. 1. Al was deposited on the oxide to form the gate electrode with an area of $3 \times 10^{-2} \text{ cm}^2$.

When the Si spacer is smaller than the correlation length, the grown Ge QDs can be self-assembled in a row vertically [9]. However, in this study, the Si spacer is 80 nm thick, which is too high to have the strain field coupling between quantum dot layers. The Ge dot is not necessarily aligned vertically in a row in our samples, as indicated in the TEM micrograph in Fig. 1.

Fig. 3 shows the I – V characteristics of the NMOS QDIP at different temperatures. At inversion bias, one component of the dark current of MOS tunneling diode is dominated by the thermal generation of electron–hole pairs from the valence to the conduction band through the defects in the depletion region and at the Si/SiO₂ interface (the inset of Fig. 3). Thermally generated electron–hole pairs reduce as the operating temperature decreases. The other component of the dark current arises from the holes thermally excited from the quantum dots to the valence band edge (the inset of Fig.

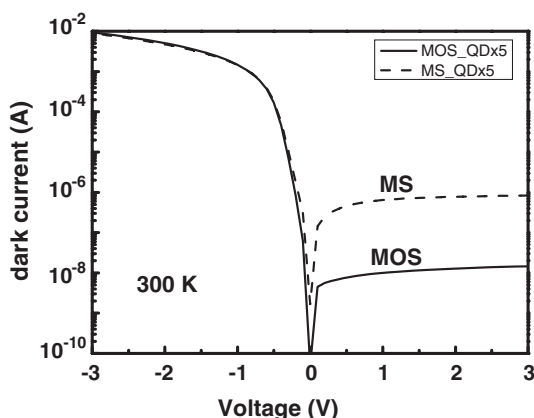


Fig. 2. Comparison of dark current between MOS and MS structures.

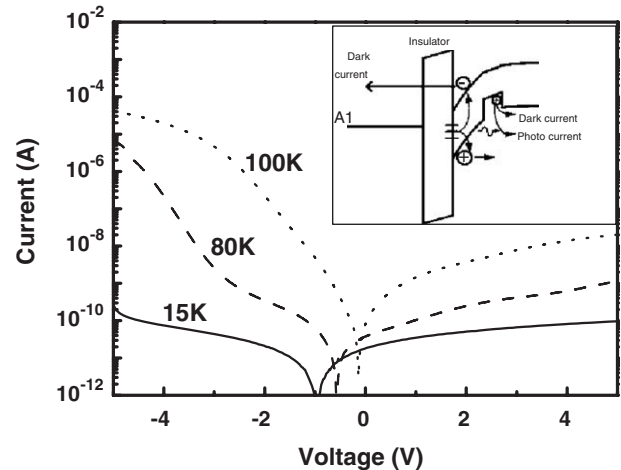


Fig. 3. Dark current of a MOS Ge/Si QDIP at different temperatures. The inset shows the band diagram of a NMOS Ge/Si QDIP at inversion bias. The confined holes can be excited under infrared exposures.

3). The dark current at the inversion bias decreases as the operating temperature reduces. At accumulation bias, the electron tunnels from the Al gate to the p-Si, and the accumulated holes at oxide/Si interface also tunnel to the Al gate electrode. Both tunneling mechanisms are related to the trap-assisted tunneling (Frenkel-Poole), and decrease with the lowering of temperature.

Under infrared exposures at an inversion bias, the confined holes can be excited and contribute to photocurrent. The spectral response is measured by Fourier transform infrared (FTIR) spectrometer (Perkin-Elmer Spectrum 2000) coupled with a cryostat [APD cryogenics] and a SR570 current preamplifier. The incident light is unpolarized and the devices are under normal incidence detection mode.

At 15 K, a broad 3.5–5 μm peak, originated from the intraband transition in the quantum dot, is observed at gate voltages of zero and 1 V with a peak responsivity of 0.03 mA/W at 1 V (Fig. 4). This intraband transition at 3.5–5 μm is different from the transition (3–10 μm) in the undoped devices, probably due to another intraband transition resulting from more holes at higher energy level. At 20 K, the responsivity of undoped-QDIPs is 0.004 mA/W at 6.6- μm peak [10]. The δ -doping is expected to contribute hole concentration in the doped devices. The dark current at 80 K for the δ -doped device

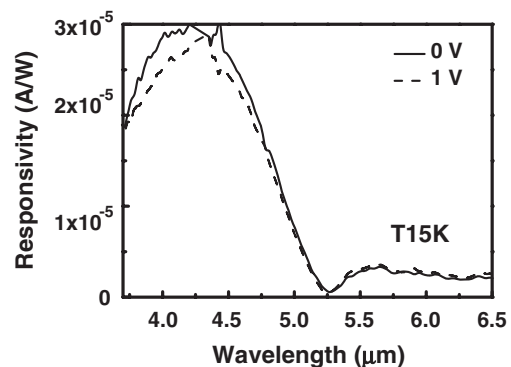


Fig. 4. Spectral response of a QD device at different gate voltages.

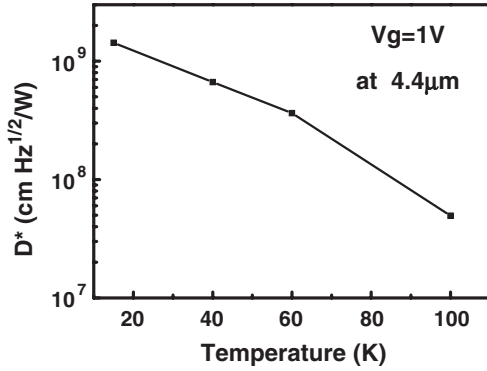


Fig. 5. The detectivity of the 3.5–5 μm peak vs. temperature at a gate voltage of 1 V for the QDIP.

is $\sim 10^{-9}$ A, which is 10 times larger than that of undoped QDIPs, because more holes can be thermally excited from the doped quantum dots. The operating temperature is also reduced due to the larger dark current. There is a trade-off between the operating temperature and responsivity.

The normalized detectivity D^* is defined as:

$$D^* = \frac{\sqrt{A\Delta f}}{\text{NEP}} = \frac{\sqrt{A\Delta f}}{i_n/R} \quad (1)$$

where A is the detector area ($3 \times 10^{-2} \text{ cm}^2$), Δf is the equivalent bandwidth of the electronic system. The noise equivalent power (NEP) is defined as i_n/R , where i_n is the current noise and R is the responsivity. The current noise is limited by the dark current and can be approximated as the shot noise $(2eI_d\Delta f)^{1/2}$, where I_d is the measured dark current. Therefore, D^* can be simplified to

$$D^* = \frac{\sqrt{AR}}{\sqrt{2eI_d}}. \quad (2)$$

Fig. 5 shows the detectivity at different temperatures at 1 V bias. The peak detectivity is found to be $10^9 \text{ cm-Hz}^{1/2}/\text{W}$ for the 3.5–5 μm peak. The detectivity decreases with the increase of operating temperature due to the rise of the dark current. For

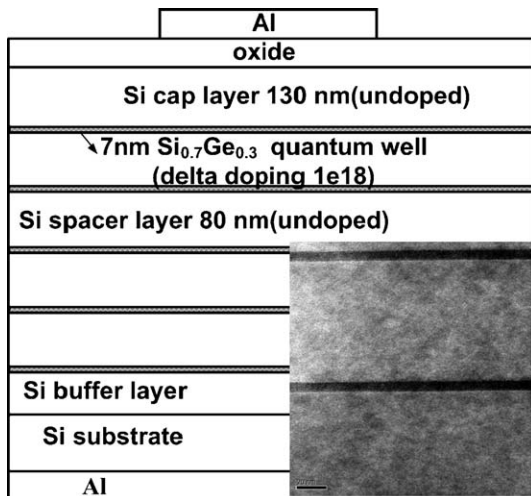


Fig. 6. The structure of the MOS $\text{Si}_{0.7}\text{Ge}_{0.3}$ QWIP. The inset shows the TEM photograph of the quantum well structure.

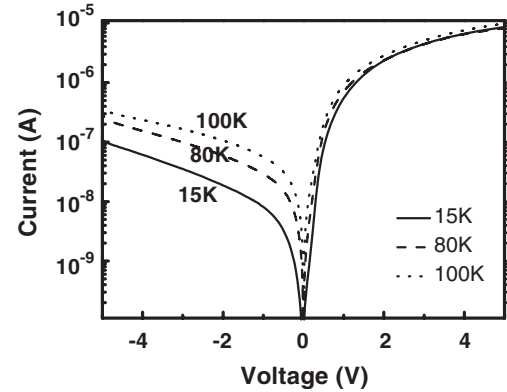


Fig. 7. Dark current of MOS QWIP devices as a function of operating temperature.

comparison, the detectivity of III–V based-ODIP (InGaAs/AlGaAs quantum well on GaAs substrates) is $4 \times 10^{10} \text{ cm-Hz}^{1/2}/\text{W}$ for 4.5 μm peak at 95 K [11].

3. δ -Doped quantum well infrared photodetector

The δ -doping was also introduced in the MOS $\text{Si}_{0.7}\text{Ge}_{0.3}$ quantum well infrared photodetector (QWIP). The structure is similar to the QD device, but the QDs are replaced by 5 layers of 7-nm-thick $\text{Si}_{0.7}\text{Ge}_{0.3}$ QWs with 80 nm spacers (Fig. 6). Boron with the concentration of 10^{18} cm^{-3} was introduced during the growth of $\text{Si}_{0.7}\text{Ge}_{0.3}$ quantum wells and the same incorporation time with the δ -doped QDIP mentioned above. The TEM photograph of the QW structure is shown in the inset of Fig. 6.

In comparison, the dark current of the δ -doped QW device (Fig. 7) is larger than that of the δ -doped QD device at low temperatures. Due to the smaller confinement energy for holes in SiGe QW, holes can be easily thermally excited and contribute to the dark current. The continuum of the two-dimensional density of states in quantum wells also assists the thermal excitation of holes out of the quantum well, as compared to the discrete energy states in quantum dots.

The spectral response of δ -doped QWIP at 15 K for different gate voltages is shown in Fig. 8. Due to the smaller

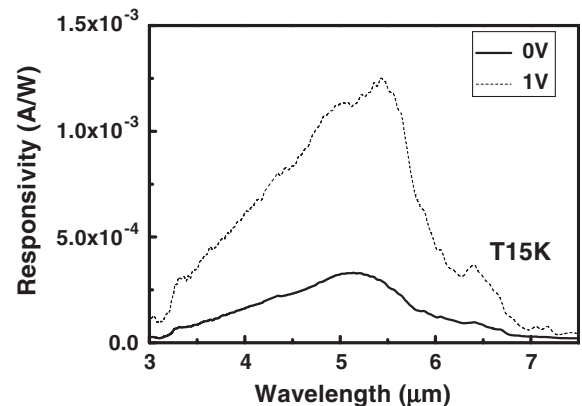


Fig. 8. Spectral response of a QW device at different gate voltages. For $V_G = 1$ V, the peak responsivity at 15 K is 1.3 mA/W.

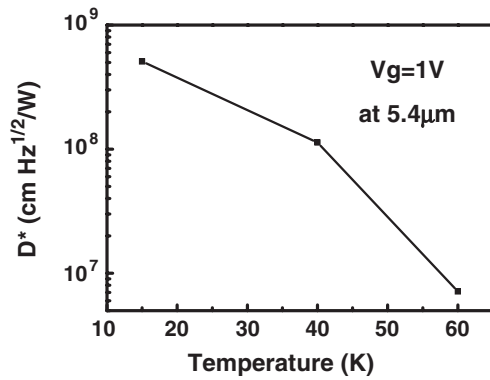


Fig. 9. The detectivity of the 3–7 μm peak vs. temperature at $V_G=1$ V for the QWIP. The response becomes weak beyond 60 K.

confinement energy of the SiGe QW device, the absorption wavelength shifts to longer wavelength (3–7 μm). For $V_G=1$ V, the peak responsivity at 15 K is 1.3 mA/W. The SiGe δ -doped QW detector has larger responsivity than that of the δ -doped QD detector. Photo-excited holes in the detectors may be trapped by subsequent layers of quantum dots/quantum wells. Trapped holes in the QW device are more easily thermally excited due to a small transition energy. This may lead to the larger responsivity as compared to the δ -doped QD device, but the exact origin is still under investigation.

The detectivity at different temperatures at 1 V bias is plotted in Fig. 9. The peak detectivity is 5×10^8 cm-Hz^{1/2}/W at 5.4 μm and decreases with increasing temperature. Due to the larger dark current, the operating temperature of the QW device is lower than that of the QD device.

4. Conclusion

MOS-based Ge/Si quantum dot/well photodetectors are demonstrated by introducing δ -doping using UHVCVD. For QDIP, a peak in wavelength range 3.5–5 μm , which originates from the intraband transition in the quantum dot, is observed.

At 15 K, the peak 3.5–5 μm responsivity is 0.03 mA/W at 1 V, and the operating temperature of the device is up to 100 K. A higher peak responsivity is observed for the δ -doped QWIP with the highest value reaching 1.3 mA/W at 1 V. The absorption region for the devices is 3 to 7 μm . However, due to larger dark current, the operating temperature of the QW device is only up to 60 K.

Acknowledgment

This work is supported by U.S. Air Force Office of Scientific Research/AOARD under contract no. FA520904P0441, and National Science Council, Taiwan.

References

- [1] Min Yang, Jeremy Schaub, Dennis Rogers, Mark Ritter, Ken Rim, Jeffrey Welser, Byeongju Park, International Electron Device Meeting, 2001, p. 547.
- [2] J. Kolodzey, T.N. Adam, R.T. Troeger, P.-C. Lv, S.K. Ray, G. Looney, A. Rosen, M.S. Kagan, Irina N. Yassievich, "The Design and Operation of TeraHertz Sources Based on Silicon Germanium Alloys," Topical Meeting on Silicon Monolithic Integrated Circuits in RF Systems, 9–11th April, 2003, Grainau, Germany.
- [3] A.I. Yakimov, A.V. Dvurechenskii, A.I. Nikiforov, Yu. Yu. Proskuryakov, J. Appl. Phys. 89 (2001) 5676.
- [4] R. People, J.C. Bean, C.G. Bethea, S.K. Sputz, L.J. Peticolas, Appl. Phys. Lett. 61 (1992) 1122.
- [5] A. Rogalski, J. Appl. Phys. 93 (2003) 4355.
- [6] R.P.G. Karunasiri, J.S. Park, Y.J. Mii, K.L. Wang, Appl. Phys. Lett. 57 (1990) 2585.
- [7] C.W. Liu, M.H. Lee, C.F. Lin, I.C. Lin, W.T. Liu, H.H. Lin, Technical Digest, International Electron Device Meeting, Washington, D.C., 1999, p. 749.
- [8] B.-C. Hsu, S.T. Chang, C.-R. Shie, C.-C. Lai, P.S. Chen, C.W. Liu, International Electron Device Meeting, 2002, p. 91.
- [9] O.G. Schmidt, K. Eberl, Phys. Rev. B. 61 (2000) 13721.
- [10] B.-C. Hsu, C.-H. Lin, P.-S. Kuo, S.T. Chang, P.S. Chen, C.W. Liu, J.-H. Lu, C.H. Kuan, IEEE Electron Device Lett. 25 (2004) 544.
- [11] A. Fiore, E. Rosencher, P. Bois, J. Nagle, N. Laurent, Appl. Phys. Lett. 64 (1994) 478.

Low-temperature fabrication and characterization of Ge-on-insulator structures

C.-Y. Yu, C.-Y. Lee, and C.-H. Lin

Department of Electrical Engineering, National Taiwan University, Taipei, Taiwan 106, Republic of China and Graduate Institute of Electronics Engineering, National Taiwan University, Taipei, Taiwan 106, Republic of China

C. W. Liu^{a)}

Department of Electrical Engineering, National Taiwan University, Taipei, Taiwan 106, Republic of China and Graduate Institute of Electronics Engineering, National Taiwan University, Taipei, Taiwan 106, Republic of China and National Nano Device Laboratories, Hsiuchu, Taiwan, R.O.C.

(Received 19 December 2005; accepted 22 July 2006; published online 7 September 2006)

Ge-on-insulator structures have been fabricated by wafer bonding and layer transfer techniques. Ultralow bonding temperatures of 150–300 °C are employed in order to suppress hydrogen outdiffusion and to produce a low defect density, in an attempt to produce high photocurrent and photoresponse. Thus reducing the hydrogen outdiffusion results in decreased surface roughness. A low defect density is suggested by a low inversion-current leakage of the tunnel diodes. The photoresponse of the Ge-on-insulator detector is also found to increase with decreasing bonding temperature, indicating that defects caused by hydrogen implantation are passivated more effectively. © 2006 American Institute of Physics. [DOI: 10.1063/1.2347116]

As channel lengths of metal-oxide-semiconductor field-effect transistors (MOSFETs) are deeply scaling down, carrier mobility enhancement in the channel is desired for improving the performance of circuitry. To achieve this purpose, germanium (Ge) is a promising channel material for MOSFETs because it has high electron and hole mobilities as compared with Si.^{1–3} A Si-on-insulator structure can improve the performance of complementary metal-oxide semiconductor circuits, due to the reduction of parasitic capacitance. Ge-on-insulator (GOI) structures may thus be particularly suitable for obtaining high-performance MOSFET devices benefiting from both the advantages of mobility enhancement and low parasitic capacitance.^{4,5} The layer transfer technique using wafer bonding and hydrogen implantation (also called smart cut^{6,7}) enables the fabrication of GOI structures. Recently, a GOI structure fabricated by a smart-cut process with low thermal budget (~400 °C) has been reported.⁸ In this letter, the fabrication of GOI structures has been demonstrated at ~150 °C: so far, a lowest GOI process temperature that has been reported. Effects of hydrogen on low-temperature GOI fabrication process have several advantages with smoother cleaved surface and defect passivation beside the low mismatch of thermal expansion reported previously.⁹

The basic fabrication process of GOI metal-insulator-semiconductor (MIS) detector involves hydrogen ion implantation and direct wafer bonding techniques. The Sb-doped *n*-type Ge substrate (001) is prepared as a “host” wafer. Then, hydrogen ions with a dose of $1 \times 10^{17} \text{ cm}^{-2}$ and an energy of 200 keV are implanted into the host Ge wafer before bonding to form a deep weakened layer. On the other substrate, thermal oxide with a thickness of 80 nm is grown on the *p*-type Si substrate to form a “handle” wafer. The handle wafer and the host wafer were hydrophilically cleaned

by using $\text{NH}_4\text{OH}:\text{H}_2\text{O}_2:\text{H}_2\text{O}$ solution and $\text{KOH}:\text{H}_2\text{O}$ solution, respectively. Then, both wafers were rinsed in deionized water and initially bonded at room temperature.^{10,11} The wafer pair was annealed to strengthen the chemical bonds between the two faces and to induce layer transfer along the weakened hydrogen-implanted region by H_2 blistering. Metal/oxide/Ge tunneling diodes were fabricated for electrical measurements. Low-temperature (~50 °C, lower than the bonding temperature) liquid phase deposition (LPD) was used to deposit the gate oxide; this process has the advantages of low cost, selective growth, and high throughput. The thickness of the LPD oxide was ~1.6 nm. Platinum (Pt) as a gate electrode was evaporated on the LPD oxide and large aluminum (Al) pad as an Ohmic contact electrode was evaporated on the same side. A cross-sectional transmission electron micrograph of a GOI metal/oxide/Ge diode is shown in Fig. 1.

The hydrogen can diffuse out from the surface during the bonding process, especially at the instant of breakage. According to published experimental result,¹² hydrogen is a fast diffuser in Ge. A lower process temperature produces a more concentrated hydrogen profile because of the low diffusion coefficient of hydrogen at low temperature. The concentrated hydrogen region would lead to a smooth cleaved surface since the separation along the microcavity plane during the smart-cut process is generated by the hydrogen bubbling near the peak implantation region. Figure 2 shows the surface roughness of the GOI sample as a function of process temperatures, measured by atomic force microscopy (AFM) on $1 \times 1 \mu\text{m}^2$ area. The surface roughness continues to decrease with decreasing process temperature. A root-mean-square (rms) roughness of ~7 nm is obtained after the H_2 blistering at 150 °C for 12 h, while the rms roughness is as high as ~27 nm after blistering at 300 °C for the same time.

During thermal treatment, the implanted hydrogen ions can passivate the defects generated by implantation damage in the Ge. At a lower bonding temperature, the outdiffusion

^{a)} Author to whom correspondence should be addressed; electronic mail: chee@cc.ee.ntu.edu.tw

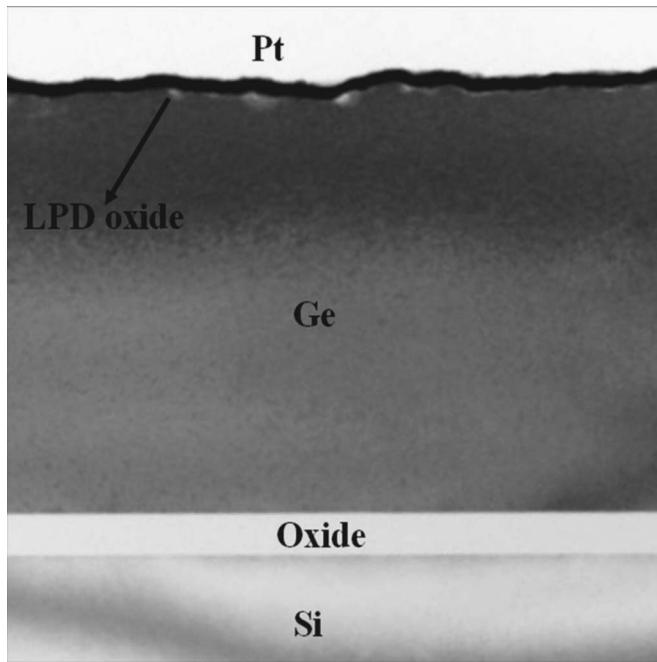


FIG. 1. Cross-sectional transmission electron micrograph of GOI MIS detector.

of hydrogen ions from the wafers can be suppressed and more hydrogen can passivate the defects. Figure 3 shows the tunneling current of Pt/oxide/GOI (MIS) diodes as a function of processing temperature. The inset of Fig. 3 is a typical current-voltage curve, for the GOI diode fabricated at 150 °C. A drop in leakage current was observed for a bonding temperature of 150 °C. The leakage current of MIS tunneling diodes at inversion bias (negative bias for *n*-type Ge) is dominated by thermal generation of electron-hole pairs through defects in the depletion region and at the Ge/oxide interface (Fig. 4).¹³ The lower defect density for the 150 °C bonding temperature is probably due to the hydrogen passivation of defects generated by hydrogen implantation. The wafer holder was cooled down to -20 °C during the implantation process. The heating due to the ion implantation may increase the wafer temperature, but the Ge substrate tempera-

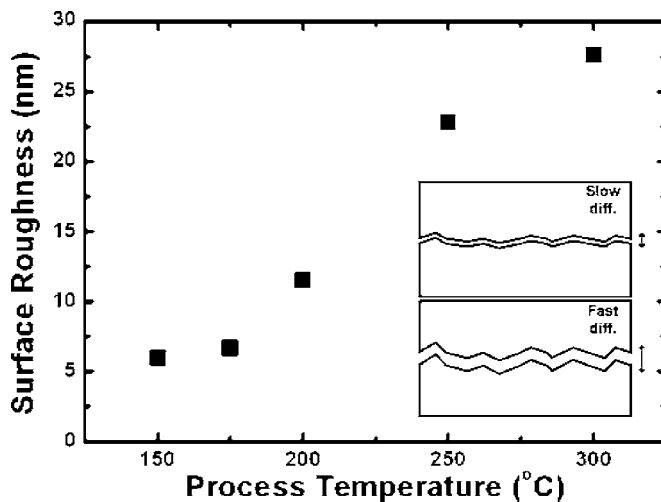


FIG. 2. Surface roughness (rms) measured by AFM as a function of process temperature. The surface roughness of the Ge-on-insulator structure decreases as the process temperature decreases (rms roughness ~7 nm at 150 °C vs ~27 nm at 300 °C).

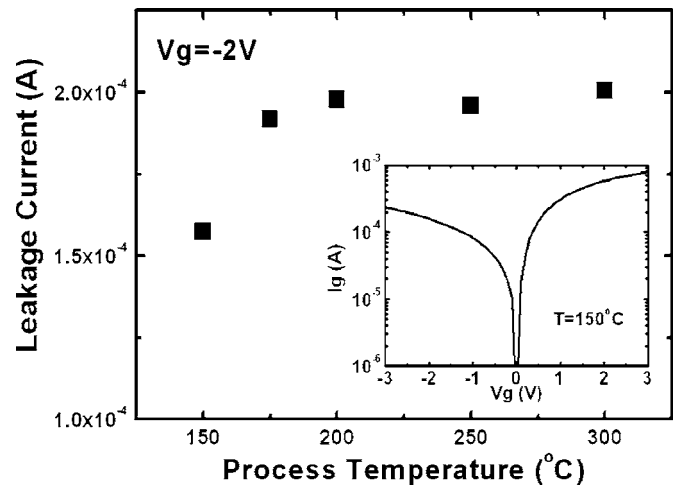


FIG. 3. Leakage current of a Pt/oxide/GOI detector with different process temperatures at inversion bias of -2 V. Typical current-voltage curves (inset) for the Ge-on-insulator MIS diode fabricated at ~150 °C.

ture is estimated to be lower than ~50 °C. No blistering was observed after the hydrogen implantation in the sample, indicating that the wafer temperature is low enough. Due to the equipment limit, the wafer holder temperature cannot be even lower.

Figure 5 shows the photoresponse of GOI MIS diode under light exposure at a wavelength of 850 nm with different bonding temperatures.¹⁴ The fiber is pointed to the edge of the gate electrode and photogenerated carriers can be collected by lateral diffusion and drift mechanisms. The photo-generated holes and electrons in the deep depletion region are separately swept towards the Pt and Al electrodes, respectively, to form the photocurrent. The responsivity increases from 3.6 to 220 mA/W as the process temperature decreases from 300 to 150 °C. Since the Ge surface is passivated by LPD oxide (the inset of Fig. 5), the surface current seems to be minimized. Surface defects in GOI near the LPD oxide can act as recombination centers, and the photogenerated electron-hole pairs can recombine at surface defects, reducing the photocurrent. Therefore, the photocurrent is more sensitive to the surface defects than the dark current. Figure 5 shows a clear trend of decreasing photocurrent with increasing bonding temperature, suggesting a concomitant

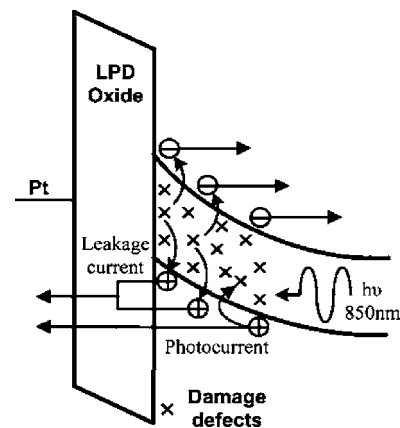


FIG. 4. Band diagram of the *n*-type GOI detector under inversion bias. The defects due to ion implantation were formed in Ge around the implanted hydrogen profile and can act as traps to reduce the photocurrent.

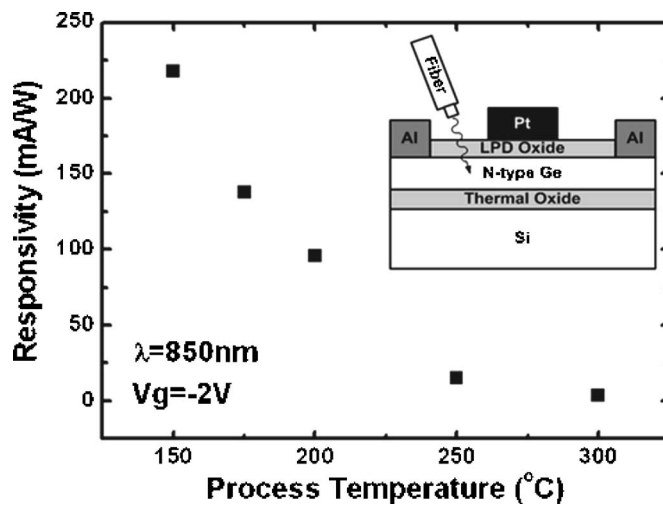


FIG. 5. Responsivity of GOI MIS detectors under light exposure at a wavelength of 850 nm for different process temperatures. The responsivity increases as the process temperature decreases. The inset shows the device structure of the GOI MIS detector.

increase in the surface defect density due to the release of hydrogen at high bonding temperatures.

In summary, GOI MIS detectors were fabricated by wafer bonding and layer transfer techniques at low temperatures. The surface roughness of GOI structure decreases as the process temperature decreases due to the suppression of hydrogen diffusion in the Ge, resulting in a smooth cleaved surface. The photoresponse of the GOI MIS detector is enhanced for lower bonding temperatures, due to the suppression of defects. Low-temperature bonding is thus a promis-

ing technique to provide GOI wafers with low defect density for future electrical and optoelectronic applications.

This work was supported by National Science Council of ROC under Contract Nos. 94-2622-E-002-010-CC3 and 94-2623-7-002-020-AT, and by U.S. Air Force Office of Scientific Research/AOARD. The proof read by Dr. Temple and Dr. Maikap is highly appreciated.

- ¹C. O. Chui, S. Ramanathan, B. B. Triplett, P. C. McIntyre, and K. C. Saraswat, *IEEE Electron Device Lett.* **23**, 473 (2002).
- ²W. P. Bai, N. Lu, J. Liu, A. Ramirez, D. L. Kwong, D. Wristers, A. Ritenour, L. Lee, and D. Antoniadis, *Tech. Dig. VLSI Symp.* **2003**, 121.
- ³H. Shang, H. Okorn-Schmidt, J. Ott, P. Kozlowski, S. Steen, E. C. Jones, H.-S. P. Wong, and W. Hanesch, *IEEE Electron Device Lett.* **24**, 242 (2003).
- ⁴Y. Liu, M. D. Deal, and J. D. Plummer, *Appl. Phys. Lett.* **84**, 2563 (2004).
- ⁵S. Takagi, *Tech. Dig. VLSI Symp.* **2003**, 115.
- ⁶M. Burel, *Electron. Lett.* **37**, 1201 (1995).
- ⁷Y. Cho and N. W. Cheung, *Appl. Phys. Lett.* **83**, 3827 (2003).
- ⁸D. S. Yu, A. Chin, C. C. Liao, C. F. Lee, C. F. Cheng, M. F. Li, W. J. Yoo, and S. P. McAlister, *IEEE Electron Device Lett.* **26**, 118 (2005).
- ⁹V. Dragoi, M. Alexe, M. Reiche, and U. Gosele, *Proceedings of the IEEE International Semiconductor Conference*, 5–9 October 1999, Vol. 2, p. 443.
- ¹⁰C.-Y. Yu, P.-W. Chen, S.-R. Jan, M.-H. Liao, K.-F. Liao, and C. W. Liu, *Appl. Phys. Lett.* **86**, 011909 (2005).
- ¹¹Q.-Y. Tong and U. Gosele, *Semiconductor Wafer Bonding* (Wiley, New York, 1999).
- ¹²O. Madelung, *Data in Science and Technology: Semiconductors* (Springer, New York, 1991).
- ¹³C.-H. Lin, B.-C. Hsu, M. H. Lee, and C. W. Liu, *IEEE Trans. Electron Devices* **48**, 2125 (2001).
- ¹⁴M. H. Liao, C.-Y. Yu, C.-F. Huang, C.-H. Lin, C.-J. Lee, M.-H. Yu, S. T. Chang, C.-Y. Liang, C.-Y. Lee, T.-H. Guo, C.-C. Chang, and C. W. Liu, *Tech. Dig. Ser.-Opt. Soc. Am.* 1001 (2005).